

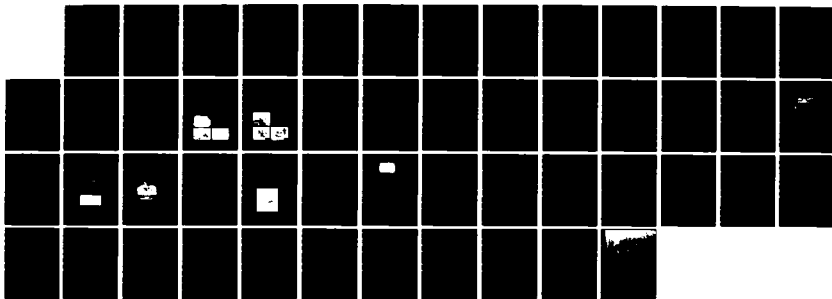
AD-A132 847

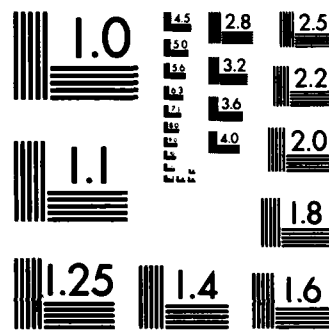
EFFECT OF CONTACT DAMAGE ON THE STRENGTH OF CERAMIC  
MATERIALS(U) NATIONAL BUREAU OF STANDARDS WASHINGTON DC  
S M WIEDERHORN ET AL. OCT 82 N00014-81-F-0002

1/1

UNCLASSIFIED

F/G 11/2 NL





MICROCOPY RESOLUTION TEST CHART  
NATIONAL BUREAU OF STANDARDS-1963-A

12

AD-A132847

Effect of Contact Damage on the Strength  
of Ceramic Materials

S. M. Wiederhorn, B. R. Lawn, E. R. Fuller, Jr.,  
B.J. Hockey, D.E. Roberts and J.S. Nadeau

Technical Report

ONR Contract No. N00014-81-F-0002  
NBS Project No. 5610453

for

Office of Naval Research  
Arlington, VA 22217

by

National Bureau of Standards  
Washington, DC 20234

October 1982

DTIC  
SEP 23 1983  
S A

This document has been approved  
for public release and sale; its  
distribution is unlimited.

DTIC FILE COPY

88 08 21 06 0

## Introduction

Work on this program during the past year has been directed towards:  
(1) analysis of surface damage that occurs during sliding contact; (2) measurement at elevated temperatures of friction between ceramics; (3) investigation of point and line damage that occurs during sharp contact.

## Surface Damage Studies

The surface damage studies were conducted on the same equipment that was developed on this program to study strength degradation. The equipment is designed to measure the sliding coefficient of friction of a sphere against a flat specimen, and is capable of operating at temperatures as high as 800°C. With modification, the equipment is capable of operating at temperature up to 1500°C.

Initial studies were conducted on soda-lime silica glass. Examination of the wear tracks indicates that plastic flow occurs at all temperatures when glass slides upon glass. As the temperature is increased the zone of plastic flow and the friction are observed to increase, primarily as a result of plowing of the glass sphere through the glass specimen. At elevated temperatures crack formation is most severe at the point where sliding initiates. The size of the crack can be correlated with the higher frictional forces required to initiate sliding at elevated temperatures. At the fictive temperature large cracks are observed at the start of the wear track; however, little or no cracking is observed along the wear track. By contrast, crack formation is much more uniform along the wear track at room temperature. The relevance of the crack formation to the strength of the glass is currently being studied.

### Friction Data

Friction data were obtained from a plate on plate apparatus that was built to measure friction where mechanical damage does not occur during sliding. Results from the apparatus indicate that the coefficient of friction between two solids increases dramatically as the temperature is increased to levels at which molecular transport can occur easily. For soda-lime silica glass and a 70 percent lead silica glass, the coefficient of friction was  $\sim 0.3$  from room temperature to  $\sim 200^\circ\text{C}$  below the fictive temperature. As the temperature increased the coefficient of friction increased to  $\sim 1$  at the fictive temperature of the glass and then decreased again at higher temperatures. Studies on silica glass, aluminum oxide and silicon nitride (NC 132) gave no indication of such dramatic behavior because of the higher temperatures needed for molecular transport. This part of the work was conducted by John S. Nadeau, who was partially supported by this contract during the past year.

Studies using glass spheres on soda-lime silica glass gave indications of a similar increase in the coefficient of friction. This increase could not be attributed to adhesion effects since measurements using normally loaded glass spheres against flat plates gave no indication of adhesion until the temperature exceeded the fictive temperature of the glass. Apparently, tangential as well as normal forces are needed for the observed frictional effects.

### Point and Line Damage

Studies of rate effects on hardness of materials were conducted using a dynamic hardness machine that was constructed in an earlier part of the ONR program. Tests were applied to single crystal copper, to polycrystalline

tungsten and to soda lime silica glass. The contact times ranged from  $\sim 10$  ms to  $10^3$  s. A distinct decrease in hardness was observed over this range: 12.5% for copper; 13.3% for glass; 21.3% for tungsten. The results of this study have been accepted for publication in the Journal of Materials Science (Letters).

In addition to the above, a theory was formulated for the general fatigue response of flaws in brittle materials to residual contact stresses associated with both point and line indentations. These residual stresses can play a dominant role in the ensuing failure mechanics. Analytical solutions were obtained for the specific case of static fatigue. The resulting relation between lifetime and failure stress has the same power-law form as the conventional solution for residual stress free flaws. However, while the form of the lifetime relation remains invariant, the values of the exponents and coefficients depend on the type of flaw (line versus point flaw) and on the presence of residual stresses. Explicit conversion formulae are given to transform "apparent" velocity parameters into "true" parameters. This work has been submitted for publication in the Journal of the American Ceramic Society.

Accession No.	
Author	
Title	
<i>Letter on file</i>	
Classification	
Subject Codes	
Date	08/00
Special	
A	

### Technical Articles

1. S.M. Wiederhorn and B.J. Hockey, "Effect of Material Parameters on the Erosion of Brittle Materials," J. Mat. Sci. 18, 766-780 (1983).
2. B.R. Lawn and S.M. Wiederhorn, "Contact Fracture in Brittle Materials," pp. 133-147 in Contact Mechanics and Wear of Rail/Wheel Systems, J. Halousek, R.V. Dukupati and G.M.L. Gladwell, eds., University of Waterloo Press, 1982.
3. C.J. Fairbanks, R.S. Polvani, S.M. Wiederhorn, B.J. Hockey and B.R. Lawn, "Rate Effects in Hardness," J. Mat. Sci. Letters, 1, 391-393 (1982).
4. E.R. Fuller, B.R. Lawn and R.F. Cook, "Theory of Fatigue for Brittle Flaws Originating from Residual Stress Concentrations," J. Am. Ceram. Soc. 66, 314-321 (1983).

1. S.M. Wiederhorn and B.J. Hockey, "Effect of Material Parameters on the Erosion of Brittle Materials," J. Mat. Sci. 18, 766-780 (1983).

# Effect of material parameters on the erosion resistance of brittle materials

S. M. WIEDERHORN, B. J. HOCKEY  
*National Bureau of Standards, Washington, DC 20234, USA*

Erosion data are compared with two theories that have been suggested to explain the erosive behaviour of solids. A dimensional analysis is applied to the variables that are important to erosion, and a multivariate, linear regression analysis is used to fit the data to the dimensional analysis. The results of the linear regression analyses are compared with the two theories in order to evaluate the applicability of these theories to erosion. Although semi-quantitative agreement of the data with the theories is obtained, some discrepancies are apparent. In particular, the dependence of erosion rate on hardness and critical stress intensity factor is greater than predicted by either of the two theories. These discrepancies are attributed primarily to microstructural aspects of erosion that are not modelled by either of the theories.

## 1. Introduction

Erosion of brittle materials by hard, solid particles is a complex process in which material is lost from the target surface by brittle fracture [1, 2]. The sizes and types of cracks that form in the target surface during impact have been studied extensively and have been shown to depend on several factors: these include particle shape, mass and velocity, and target material hardness and toughness. At low velocities well-developed crack systems form at the impact site: cone cracks are formed by rounded ("blunt") particles [3-5], lateral and medium cracks by angular ("sharp") particles [3, 6-8]. At extremely high velocities the appearance of the impact surface is affected by the ejection of material from the target surface as the particle plows into the surface, and by severe cracking and chipping of the surface after the particle has left the impact site [1, 4, 9, 10]. The types of crack systems that are formed during impact and the conditions that control their formation have been discussed extensively in the references cited above.

Plastic deformation also plays an important role in the erosion process. Thus, a detailed examination of impact sites in brittle materials indicates that a zone of intense plastic deformation

forms during contact, beneath the immediate area of the contact [7, 11-13]. Residual stresses associated with the plastic zone force small cracks, known as lateral cracks, to grow from the impact site. Initially, these cracks grow parallel to the target surface, but then curve towards and eventually intersect with the surface resulting in a loss of material from the target. Because of this behaviour, the erosion process in brittle materials is viewed by many investigators as an elastic-plastic event, the plastic deformation at the impact site being the prime driving force for the surface fracture that results in material loss during erosion [1, 2, 10]. While this view of erosion may be over simplified considering the complexity of the process, it has been used to model the erosion process and to develop equations that predict erosion rates as a function of projectile and target parameters that are known to influence the erosion process in brittle materials.

Two elastic-plastic theories have been developed to explain the erosion of brittle solids. Both are based on the assumption that lateral cracks grow in a quasi-static manner as a result of residual stresses introduced by the impact event. In both theories, the size of the lateral cracks,  $c$ , are assumed to be determined by the following

relation [14]\*:

$$P/c^{3/2} = \beta K_c \quad (1)$$

where  $P$  is the maximum normal load during impact,  $K_c$  is the critical stress intensity factor, and  $\beta$  is a nondimensional constant. The volume of material removed during erosion,  $V$ , is determined from the size of the lateral crack,  $c$ , and the depth of the crack,  $d$ , beneath the target surface

$$V = \pi c^2 d. \quad (2)$$

Since the impact sites are assumed to be non-interacting, the total wear volume,  $W$ , is just the summation of the volumes resulting from the individual impact events.

The two elastic-plastic wear theories differ in their assumed dependence of impact load,  $P$ , on the kinetic and material parameters that are important to erosion. The theory developed by Evans *et al.* [10] includes dynamic stress wave effects in the calculation of  $P$ . A spherical particle is assumed to penetrate into a target without distortion; the contact pressure is assumed to be equal to the dynamic pressure that occurs when the particle first hits the target surface. The depth of penetration is determined from the time of contact and the mean interface velocity, both of which are calculated from a one-dimensional analogue. The final expression for the erosion rate,  $W$ , is

$$W \propto v_0^{3.2} R^{3.7} \rho^{1.6} K_c^{-1.3} H^{-0.25} \times [(Z_t Z_p)^{2/3} / (Z_t^{1/2} + Z_p^{1/2})^{5/3}] \quad (3)$$

where  $v_0$  is the initial particle velocity,  $R$  and  $\rho$  are the particle radius and density, respectively,  $K_c$  and  $H$  are the target toughness and hardness, respectively, and  $Z_t$  and  $Z_p$  are the impedances for the target and the particle, respectively,  $H$  is the hardness and  $V_0$  is the initial particle velocity. The term within the brackets varies by less than 10% for the materials used in the current study, and therefore will be considered to be a constant for the purpose of this paper. Hence, the equation for the erosion rate reduces to

$$W \propto v_0^{3.2} R^{3.7} \rho^{1.3} H^{-1.25} \quad (4)$$

A quasi-static formulation of the erosion

problem is based on work by Wiederhorn and Lawn [15], in which the kinetic energy of the particle is assumed to be absorbed completely by plastic flow when a particle impacts the surface. From this assumption, both the maximum force during contact and the maximum depth of penetration can be calculated. Assuming that the lateral cracks generate at a distance beneath the surface that is equal to the maximum depth of particle penetration, the following equation for the erosion rate is derived [2]

$$W \propto v_0^{2.4} R^{3.7} \rho^{1.2} K_c^{-1.3} H^{0.11} \quad (5)$$

The forms of the two erosion theories presented above are similar in that they express the erosion process by a power law dependence of erosion rate on both particle ( $v_0$ ,  $R$ ,  $\rho$ ) and target ( $K_c$ ,  $H$ ) properties. Although the same properties are used in both theories, the exponents for velocity, particle density, and hardness differ. A comparison of these theories with experimental results on erosion indicates that the theories are reasonably consistent with experiment with regard to the exponents for velocity and particle size [2]. The effect of particle density on erosion has not been investigated in any systematic manner, so that there is no way of knowing if the exponents given in Equations 4 and 5 are correct. A study of the effect of hardness,  $H$ , and fracture toughness,  $K_c$ , on erosion has recently been conducted on a series of ceramics by Evans *et al.* [10] and by Gulden [16]. The data obtained by Evans *et al.* [10] suggest a greater dependence of erosion rate on  $K_c$  and  $H$  than is predicted by their theory. Aside from these studies, however, there have been no systematic investigations of the effect of  $K_c$  and  $H$  on the erosion rate of brittle materials.

In this paper, the erosion of dense brittle materials is studied in order to assess the validity of the erosion theories represented by Equations 4 and 5. Of particular interest to this study are the particle velocity and the material parameters  $K_c$  and  $H$ . The results of our study will show that while both theories provide a qualitative description of the erosion data, neither theory is quantitatively correct. The reason for these differences seems to lie in the simplifying assumptions made

\*This relation is concerned with the formation of radial cracks from a sharp indentation. For the relation to be valid, the crack must be large relative to the size of the indentation. The use of this relation to describe lateral crack formation is based on work by Evans *et al.* [10] who showed experimentally that the size of the two cracks were proportional. Hence, the use of Equation 1 to describe erosion phenomenon has its basis in empirical investigations, but has no theoretical justification.

TABLE I Properties of target materials used in erosion study

Material	Young's modulus (GPa)	Hardness (GPa)	Toughness, $K_{Ic}$ (MPam <sup>1/2</sup> )	Microstructure
Hot-pressed silicon nitride	317 [17]	19.9 [18]	5.0 [19]	Fully dense ~ 1 $\mu$ m grain size
Hot-pressed silicon carbide	466 [20]	29.4 [18]	4.0 [21]	Fully dense ~ 1 to 2 $\mu$ m grain size
Hot-pressed aluminium oxide	425 [22]	22.0 [18]	4.0 [23]	Fully dense ~ 3 to 4 $\mu$ m grain size
Sintered aluminium oxide	425 [22]	21.7 [18]	2.2 [24]	Fully dense ~ 30 $\mu$ m grain size
Sapphire	425 [22]	21.7 [18]	2.2 [24]	Single crystal {10 $\bar{1}$ 1} plane
Silicon	168 [25]	10.6 [18]	0.7 [26]	Single crystal {112} plane
Silica glass	75 [27]	8.7 [18]	0.77 [28]	C7940
Soda-lime-silica glass	75 [27]	6.3 [18]	0.75 [28]	C0800
Magnesium oxide	330 [22]	8.0 [29]	2.6 [18]	Fully dense ~ 10 to 15 $\mu$ m grain size

in both theories of erosion. As will become apparent, details of the microstructure and material interaction during impact affect erosion in ways not fully accounted for by the present models of erosion.

## 2. Experimental procedure

The target materials used in the present investigation provided a reasonably wide range of target properties ( $K_{Ic}$  and  $H$ ) and microstructure for study (Table I). Examination of the impact area by transmission electron microscopy showed that all of the materials selected for investigation deformed plastically when subjected to impact [13]\*. The cracks that were generated by the impacting particles, while originating from within the deformed zone, exhibited no evidence of localized plastic deformation at the crack tip, and accordingly propagated in a brittle manner†. Therefore, these materials fit within the framework of the theories discussed above.

The particles used for erosion measurements were 150  $\mu$ m SiC abrasive grains. Because of the hardness of these particles it was felt that they

simulated the hard, non-yielding particles assumed to be responsible for erosion in the theories used to derive Equations 4 and 5. To achieve a uniform particle size for investigation, all particles were sieved between an 80 and 120 mesh screen before being used in erosion investigations. The particles that were used passed through the 80 mesh screen, but were retained by the 120 mesh screen.

The erosion apparatus used in this study has been described previously [30]. Briefly, the equipment was designed to feed abrasive particles into a high velocity air stream, which propelled the particles against the specimen surface (Fig. 1). The particles were accelerated by passing them through a tungsten carbide nozzle ~ 5 cm long and 0.16 cm in internal diameter. The acceleration of the particles to high velocity is accomplished within the nozzle. The particle-air mixture is passed through a ceramic tube, 2 cm in diameter, to obtain a relatively uniform beam of abrasive particles. High temperatures can be achieved by feeding a propane-oxygen mixture through a ring-burner into the top of the ceramic tube. The high velocity particle-air

\*The technique of transmission electron microscopy was applied only to the crystalline materials used in this investigation. With regard to their deformation and fracture properties, however, other studies suggest that the behaviour of glass is similar to that of crystalline materials (see Lawn *et al.* [13] for a discussion of this point).

†With the exception of MgO for which dislocations can probably be generated at crack tips.

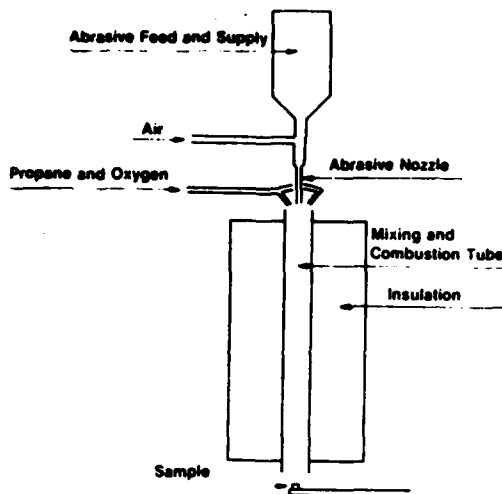


Figure 1 Schematic diagram of erosion equipment (after Wiederhorn and Roberts [30]).

stream sucks the flame from the burner into the ceramic tube to produce temperatures as high as 1200°C.

The particle velocities were measured by using a time-of-flight technique developed originally by Ruff and Ives [31]. In this technique, two discs rotate on a common axis which is parallel to the direction of the erosive gas stream. The disc closest to the exit port of the erosion apparatus contains a slit, which permits particles to pass through the disc and impinge on the second disc. For a fixed rotational speed, the position of the erosion mark on the second disc, relative to the position of the slit on the first disc, establishes the particle velocity.

The sensitivity of the double disc technique to measure particle velocities was improved during the course of the present study by mounting partially silvered glass microscope slides on the second disc directly below the slit on the first disc [32]. Particles that impinged on the glass slide formed impact damage that destroyed the reflectivity of the microscope slide in the immediate area of impact. As a consequence, the position of the erosion marks on the microscope slides were easily observed and measured. Quantitative optical microscopy was used to improve the accuracy of measuring the position of the erosion marks on the microscope slides. The original technique was further improved by first rotating the disc in one direction to obtain an erosion

mark and then in the opposite direction to obtain a second erosion mark. This procedure doubled the distance between marks, thus improving the accuracy of the velocity measurements.

The specimens used in this study were ~1.25 cm square plates approximately 0.6 cm thick. They were mounted on a support arm and held with their wide face normal to the stream of erosive particles. Specimens were exposed to a fixed mass of erosion particles, which ranged from 25 to 400 g depending on the target material and the particle velocity selected for study. The mass lost by the target during each experiment was measured to at least 1% accuracy using an analytical balance. The erosion rate was calculated from the fraction of particles that intersected the specimen. The number of particles impacting the target was estimated from the mass of abrasive used and the mean particle size of the abrasive (approximating the particles as spheres). Finally, the volume loss per particle impact (i.e. the erosion rate) was calculated from the mass lost from the specimen per particle impact, and the target density.

### 3. Results

The results of our studies are shown in Figs. 2 to 4\*. In each case the log of the erosion rate (expressed as volume lost per particle impact) is plotted against the log of the particle velocity. Fig. 2 presents the results obtained at room temperature. The erosion rate was measured for velocities ranging from 37 to 94 m sec<sup>-1</sup>, for the nine target materials used in the present study. The erosion data shown in Fig. 2 fit a power law function as expressed by Equations 4 and 5. The slopes of the curves at room temperature ranged from 1.9 for hot-pressed silicon carbide to 2.9 for silicon and silica glass. The standard error of the slopes ranged from ~0.003 to ~0.25 with a mean value of ~0.1 (Table II), which indicates that at the 95% confidence level and for two degrees of freedom, a difference in slope of ~0.4 is significant. With the exception of the hot-pressed silicon nitride, the values of these slopes are similar to those reported by other investigators on similar materials [33-38]. The slope of the hot-pressed silicon nitride was about one-half that reported earlier by Gulden [16]. The erosion rate of the target materials shown in Fig. 2 decreases as the tough-

\*The data used in these figures are summarized in Appendix B.

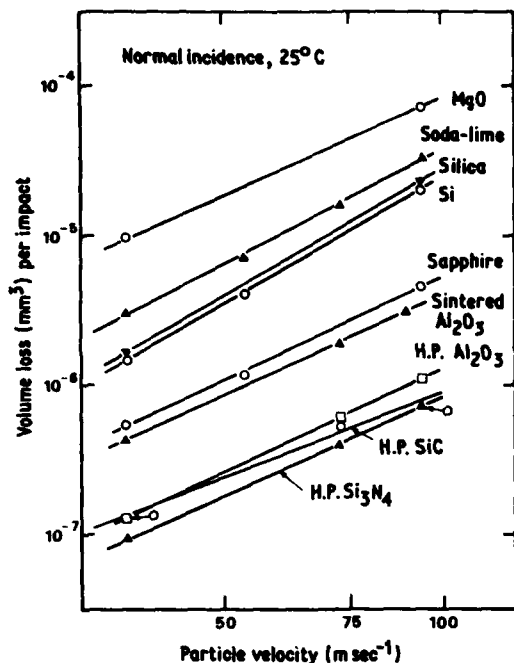


Figure 2 Erosion of brittle materials at 25°C, normal incidence impact, 150  $\mu\text{m}$  SiC particles. For clarity the errors given in Table IB have been left off the figure.

ness of the target material increases, a finding that provides qualitative support for the erosion theories described by Equations 4 and 5. A quantitative comparison of the two theories with the data will be made in a later section of this paper.

The abrasive wear data collected at 500 and 1000°C are shown in Figs. 3 and 4, respectively, for several of the target materials used in the present study. The data shown in these figures are similar to those obtained at room temperature. However, for some of the materials the slopes of the curves at elevated temperatures were significantly greater than those obtained at room temperature. Although the relative position of the erosion curves on the graph was roughly the same at elevated temperature and room temperature, small systematic differences in erosion behaviour were obtained for some of the materials. Thus, elevated temperatures appeared to slightly enhance the erosion rate of silicon, and hot-pressed silicon nitride at the higher velocities, whereas the erosion rate of glass, sapphire, and sintered aluminium oxide was reduced at the lower velocities. The results of the present study were similar to those reported earlier by the present authors on a smaller set of data [7].

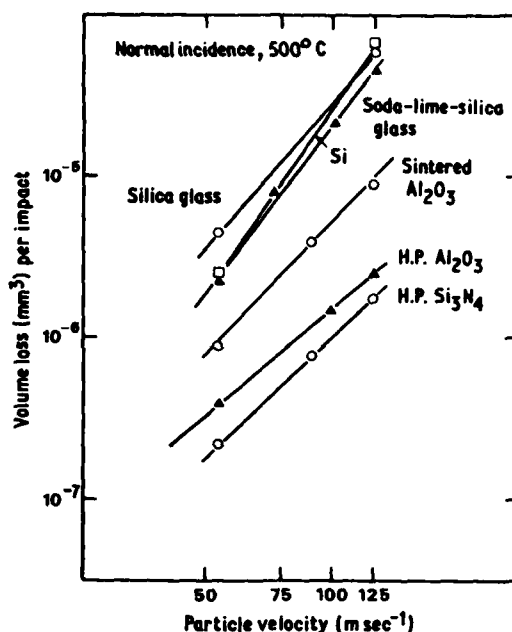


Figure 3 Erosion of brittle materials at 500°C, normal incidence impact, 150  $\mu\text{m}$  SiC particles. For clarity the errors given in Table IB have been left off the figure.

#### 4. Discussion

The purpose of this paper is to present data that can be compared with the elastic-plastic theories (Equations 4 and 5) that have been developed to explain the erosion of brittle materials. In particular the erosion data were used to evaluate the exponents of  $v_0$ ,  $K_c$ , and  $H$ , which were then compared with those given in Equations 4 and 5. Since  $K_c$  and  $H$  are determined by the properties of the target material, they cannot be varied independently, and hence have to be compared with the theories in combined form:  $K_c^{-1.3}H^{-0.25}$  for Equation 4;  $K_c^{-1.3}H^{0.11}$  for Equation 5. A second way of comparing the exponents of Equations 4 and 5 with the experimental data is by first expressing these two equations in dimensionless form through the use of a dimensional analysis and then fitting the dimensionless equation to the experimental data to obtain the exponents. Both of these techniques will be used in this paper.

##### 4.1. Velocity exponents

The velocity exponents obtained in this paper are summarized in Table II, and can be compared with other data reported in the literature for similar materials (Table III). As can be seen from these tables, data obtained in the present

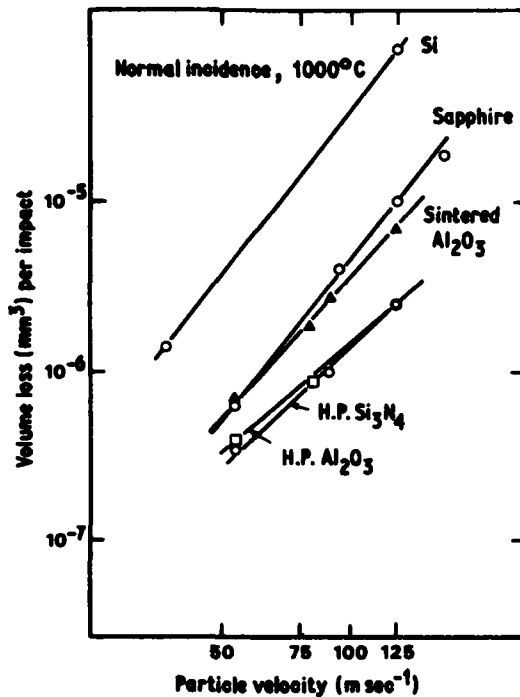


Figure 4 Erosion of brittle materials at 1000°C, normal incidence impact, 150  $\mu\text{m}$  SiC particles. For clarity the errors given in Table IB have been left off the figure.

study are reasonably consistent with those reported by other authors. Most of the differences between the results shown in Tables II and III are believed to be due to small, systematic, interlaboratory differences in experimental technique. The results on hot-pressed silicon nitride, however, differ significantly from our own because of the large

difference in velocity exponent (4 versus 2.2) obtained in the two studies.

The velocity exponents from Table II cluster more closely about the value (2.4) predicted by the quasi-static model of erosion, Equation 5, than the value (3.2) predicted by the dynamic model of erosion, Equation 4. This conclusion has to be tempered by the fact that the velocity exponent of  $v$  increases as the temperature is increased and tends to fall between the two predicted values. Furthermore, recent studies on silicon by Scattergood and Roubort [36] suggest that the velocity exponent increases as the particle size decreases. Hence, for small particles, the trend is toward better agreement between the dynamic theory of erosion and experimental measurement. These dependences of velocity exponent on temperature and on particle size are not predicted by either theory.

#### 4.2. Target parameters

The erosion data presented in Fig. 2 are compared with the material parameters  $H$  and  $K_c$  in Fig. 5. Fig. 5a compares the erosion data with the dynamic theory of erosion; Fig. 5b compares the erosion data with the quasi-static theory of erosion. With the exception of MgO, the data on both figures plot as straight lines, lending credence to the suggested theories of erosion. However, both sets of data are represented by lines with slopes greater than 1, the theoretically expected slope. The empirical slope for the dynamic erosion theory,  $\sim 1.2$ , is closer to the expected slope of 1 than is the slope,  $\sim 1.5$ , for the quasi-static theory of

TABLE II Velocity exponents for erosion data: normal incidence

Material	25° C	Temperature 500° C	1000° C
Magnesium oxide, polycrystalline	2.2	—	—
Soda-lime-silica glass	2.5 (0.12)*	3.5 (0.20)	—
Vitreous silica	2.9	3.0	—
Sapphire	2.3 (0.10)	2.4 (0.25)	3.3 (0.03)
Sintered aluminium oxide, 30 $\mu\text{m}$	2.3 (0.003)	2.8 (0.09)	2.7 (0.15)
Hot-pressed aluminium oxide, 3 to 4 $\mu\text{m}$	2.3 (0.03)	2.1 (0.04)	2.3 (0.11)
Silicon	2.9 (0.03)	3.8	3.4
Hot-pressed silicon carbide	1.8 (0.16)	—	—
Hot-pressed silicon nitride	2.1 (0.08)	2.5 (0.03)	2.4 (0.20)

\*The numbers in parentheses give the standard error for the value of the velocity exponent, which was determined by a linear regression analysis of the mean wear values given in Table IB. For exponents that were determined from only two wear values, no standard error is given.

TABLE III Velocity exponents for erosion data: normal incidence

Target material	Erosion particles	Exponent	Reference
Soda-lime-silica glass	SiC, 120 grit	3.0	[33]
MgO (96.5%)	SiC, 120 grit	2.7	[33]
Al <sub>2</sub> O <sub>3</sub> (99.5%)	SiC, 120 grit	2.6	[33]
Pyrex glass	Al <sub>2</sub> O <sub>3</sub> , 30 μm 10 μm	2.2 2.7	[34]
Hot-pressed Si <sub>3</sub> N <sub>4</sub>	SiC 8 to 940 μm	4.0	[35]
Silicon	Al <sub>2</sub> O <sub>3</sub> , 23 μm to 270 μm	3.4 to 2.6 depending on particle size	[36]
Reaction bonded SiC	Al <sub>2</sub> O <sub>3</sub> , 130 μm 270 μm	2.3 2.0	[37]
Hot-pressed SiC	Al <sub>2</sub> O <sub>3</sub> , 130 μm 270 μm	1.8 1.5	[38]

erosion. Similar values of slopes were observed by Gulden [16] in an erosion study on a different set of materials. Hence, from this type of analysis, the dynamic theory of erosion appears to provide a somewhat better fit to the erosion data than does the quasi-static theory.

The data for MgO are not consistent with the data obtained for the other materials, undoubtedly because of the type of impact damage formed in the surface of this material. The MgO cracked along the grain boundaries in the vicinity of the impact site, so that each impact event formed a loosely connected aggregate of grains that

surrounded the impact site. These damaged areas were easily removed from the surface during erosion, resulting in a higher rate of erosion than predicted theoretically. In essence, the mechanism of erosion for MgO differed markedly from that for other materials. Erosion of polycrystalline MgO probably does not fit the lateral chipping models.

#### 4.3. Dimensional analysis

Dimensional analysis [39] is an alternative method of obtaining relationships between the parameters that affect erosion. While not providing a specific

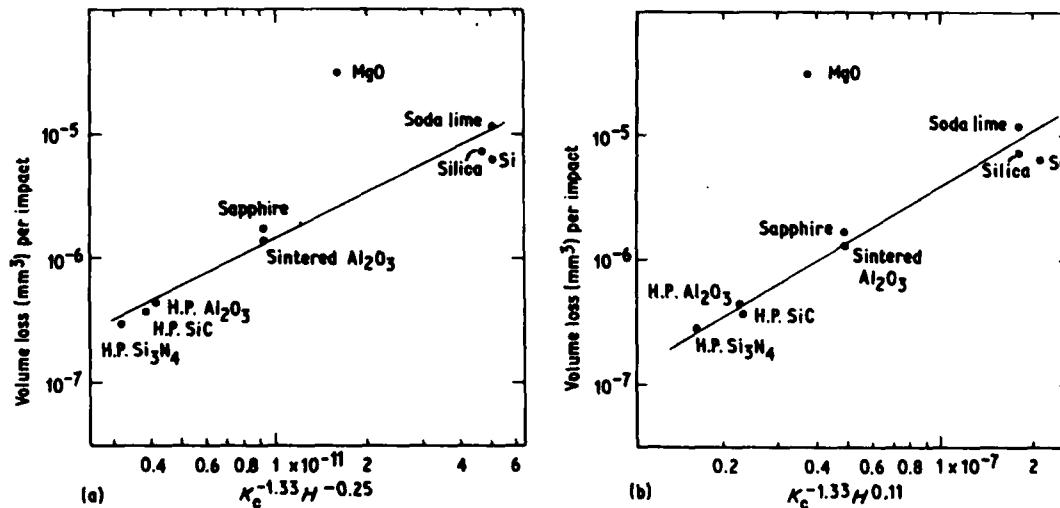


Figure 5 Comparison of the erosion data with the theories given by (a) Equation 4 [10] and (b) Equation 5 [2]. The volume lost per particle impact was selected from Fig. 2 at a velocity of 63 m sec<sup>-1</sup>. Units of hardness and toughness used to calculate the abscissae of this figure were Pa and Pam<sup>1/2</sup>, respectively.

model of erosion, dimensional analysis provides an operative equation to describe erosion in terms of dimensionless groups of variables and empirical constants determined from a regression analysis of experimental data. The empirical constants can be compared with those determined from the two erosion models to yield an unbiased comparison of theory and experiment.

To apply dimensional analysis, we assume that the parameters that control erosion are those given in Equations 4 and 5. The volume loss per particle impact,  $W$ , is then a function of these parameters:

$$W = F(v_0, R, \rho, K_c, H) \quad (6)$$

Using the standard methods of dimensional analysis [39], the following functional relation is obtained:

$$W/R^3 = A(K_c^2/RH^2)^a(\rho v^2/H)^b \quad (7)$$

where  $A$  is a dimensionless constant\*.

Because Young's modulus has been suggested as a variable that contributes to crack formation during hardness indentations [40], the treatment given above was extended to include Young's modulus,  $E$ . The equation obtained is similar to Equation 7, but contains an extra dimensionless term,  $E/H$

$$W/R^3 = A'(K_c^2/RH^2)^a(\rho v^2/H)^b(E/H)^c \quad (8)$$

Equation 7 contains three dimensionless groups each of which has physical meaning. The first represents the ratio of the volume loss during impact to the volume of the impacting particle. All other parameters being constant, the erosion rate will increase as the particle volume (i.e. particle size) increases. The second group  $(K_c^2/RH^2)$  can be represented as the ratio of the inverse of target brittleness to the size of the impacting particle. This interpretation follows from the fact that  $(K_c/H)^2$  is a measure of the relative resistance of a target to fracture during an impact event: the higher the value of  $(K_c/H)^2$ , the more resistant the target will be to fracture. The parameter  $(K_c/H)^2$  can be thought of as representing a critical scaling dimension above which fracture occurs during contact. The inverse quantity,  $(H/K_c)^2$ , is a useful index of "brittleness".

\*This equation is derived in Appendix A.

†For a definition of  $t$ , see any standard statistics text, e.g. [41].

‡This conclusion must be tempered by the fact that  $E/H$  only varied by a factor of about 2 in the present study. A larger variation of this parameter might indicate a significant dependence of wear on  $E/H$ .

[40] The third group,  $(\rho v^2/H)$  represents the ratio of the particle energy density, i.e. kinetic energy per particle volume,  $\rho v^2$ , to the hardness, which can be considered as a deformation energy density. The fourth dimensionless constant in Equation 8 can be considered as the ratio of the elastic to the plastic energy density.

The constants  $a$  and  $b$  for the dynamic model of erosion, have values of  $-0.67$  and  $1.58$ , respectively. For the quasi-static erosion model, the values of  $a$  and  $b$  are  $-0.67$  and  $1.22$ , respectively. The value of  $c$  in Equation 8 is zero for both models. Hence, the two models differ only in the exponent of the third dimensionless group.

Empirical values of the constants,  $a$ ,  $b$  and  $c$  for Equation 7 and 8 were obtained by a multiple regression analysis of the data (MgO excluded) reported in Fig. 2. The results of the analysis are given in Table IV. The statistics in this table give useful information on the relative importance of the constants  $a$ ,  $b$  and  $c$  with regard to the fit of the erosion data. Virtually the same values of  $a$  and  $b$  and their standard errors are obtained regardless of whether two or three independent variables are used for the regression analysis. The standard errors for  $a$  and  $b$  are relatively small (7 and 11% of the mean, respectively) and the values of  $t^\dagger$  computed for these constants are large and hence significant for any reasonable level of probability. By contrast, the standard error for  $c$  (55% of the mean) is large, and the value of  $t$  obtained for this constant is not significant at the 95% level, which suggests that the value of  $c$  reported in Table IV does not differ significantly from zero. From this discussion we conclude from our results that the wear rate does not depend in any significant way on the ratio of the Young's modulus to the hardness,  $E/H^\ddagger$ . This conclusion is supported by the fact that  $r^2$ , which gives the fraction of the variance accounted for by the regression analysis, only changes from 94 to 95% when  $E/H$  is added as an independent variable. Consequently, the values of  $a$  and  $b$  determined from the two parameter regression analysis will be used for purposes of further discussion in this paper.

As can be seen from Table IV, the empirical value for  $a$ ,  $-0.932$ , is greater in absolute value

TABLE IV Determination of the exponents of Equations 7 and 8 by a multivariable regression analysis (room temperature data)

Exponent	Regression coefficient	Standard error of coefficient	Computed <i>t</i>
Equation 7			
<i>a</i>	-0.932	0.110	- 8.44
<i>b</i>	1.384	0.093	14.92
Intercept, ln <i>A</i>		- 11.40	
Multiple correlation		0.971	
<i>r</i> <sup>2</sup>		0.942	
Standard error of estimate		0.415	
Equation 8			
<i>a</i>	-0.905	0.106	- 8.56
<i>b</i>	1.312	0.096	13.66
<i>c</i>	-0.669	0.364	- 1.84
Intercept, ln <i>A</i>		- 9.84	
Multiple correlation		0.975	
<i>r</i> <sup>2</sup>		0.950	
Standard error of estimate		0.415	

than the theoretical value of *a*, -0.667, given by Equations 4 and 5. The value for *b*, 1.38, lies approximately half-way between the value of 1.22 predicted by the quasi-static theory and the value of 1.58 predicted by the dynamic theory. Using the values of *a* and *b* from the multiple regression analysis, Equation 8 can be expressed in a form that is similar to that of Equations 4 and 5

$$W \propto v^{2.8} R^{3.9} \rho^{1.4} K_c^{-1.9} H^{0.48} \quad (9)$$

The most significant difference between Equations 4 and 5 and Equation 9 is the dependence of the wear rate on the fracture toughness and the hardness. The exponent of  $K_c$  suggests a stronger dependence on this value than is predicted theoretically. As  $K_c$  of the target is increased, the difficulty of removing material by chipping increases more rapidly than predicted by either theoretical treatment. Possible sources of this variation involve the effect of microstructure on erosion and the random nature of the impact process. These sources of variation imply that the models suggested to explain erosion may be too simple to account fully for the effect of fracture toughness on the erosion rate. The effect is microstructure and the random nature of the particle impact process will be discussed more fully in a later section of this paper.

In view of the fact that most theories of erosion predict a decrease in the erosion rate as the hardness is increased, the positive exponent of the hardness in Equation 9 requires some rationaliz-

ation. An explanation for the positive exponent for hardness in Equation 9 can be developed from a closer examination of the quasi-static theory of erosion. In this theory, hardness determines both the depth of penetration and the maximum load during impact. In the expression for maximum load, hardness enters the equations with a positive exponent, such that for a fixed impact energy the maximum impact load increased as the hardness is increased. Since the amount of chipping is proportional to the maximum load during impact, the relation between load and hardness suggests that the erosion rate increases as the hardness increases. Penetration is also important because it determines the depth beneath the surface where lateral cracks form: the deeper the penetration (lower hardness) the greater the erosion rate. In the final erosion equation, the penetration term and the load term oppose one another with regard to hardness and the larger of the two determines the exponent for the hardness. In Equation 5 the load term dominates, and the exponent for the hardness is positive. Using this same line of reasoning, the results of the regression analysis suggest that hardness effects surface load to a greater extent than penetration depth, resulting in a positive exponent for hardness in Equation 9. The fact that the exponent in Equation 9 is greater than 0.11 suggests that the effect of the surface load term on erosion is greater than that predicted by the quasi-static theory of erosion.

#### 4.4. Microstructural analysis of impact damage

As noted in the previous section of this paper, the large exponent of  $K_e$  in Equation 9 may have its origin in effects due either to target microstructure or to the random nature of the particle impact process. The two theories of erosion discussed in this paper are predicated on the assumption that the particles impact on sharp corners and that the type of damage is similar, regardless of the properties of the target material. If either assumption is not valid, then the dependence of erosion on  $K_e$  will differ from that given by Equations 4 and 5.

Examination of surfaces that have been impacted by small numbers of particles yields information on both the type of damage that occurs during erosion and the relative number of particles that result in chipping from the target surface. When particles impact the target, they either leave shallow, plastic impressions, or small chipped regions at the point of impact (Fig. 6). The plastic impressions are probably left by particles that were not oriented to impact on a sharp corner, but on a side, or edge. The residual plastic impressions in the target surface suggest that the deformation was not concentrated sufficiently to nucleate and

propagate surface cracks, i.e. stresses at the impact site did not exceed the threshold for fracture at these shallow impressions. Consequently, only a fraction of particles that impact the target surface are effective in the removal of material. If this fraction depends on  $K_e$ , then the erosion of the target will also depend on  $K_e$ , but in a way not given by Equations 4 and 5.

In our study of the morphology of eroded surfaces we have observed that as the toughness of the material is increased, the relative number of impacts that result in chipping is reduced, regardless of impact velocity. This observation of impact behaviour is illustrated in Fig. 6, where erosion surfaces of glass, sapphire, and silicon nitride are compared. As can be seen, the fraction of impacts that results in fracture and material removal increases as the fracture toughness of the target decreases. For glass, every impact site in Fig. 6a has resulted in crack formation. By contrast, both the sapphire and the silicon nitride have several impact sites where plastic impressions were left, but where crack formation was not apparent. This observation suggests that the functional dependence of erosion rate on  $K_e$  for brittle materials is not completely described by either theoretical treatment of erosion (Equations 4 and 5), but instead depends on factors that are related to the nucleation of cracks at the impact site. Apparently crack nucleation is relatively easier when a "blunt" impact occurs in glass or silicon, than when it occurs in the hot-pressed materials used in the present study. Hence, the rather large dependence

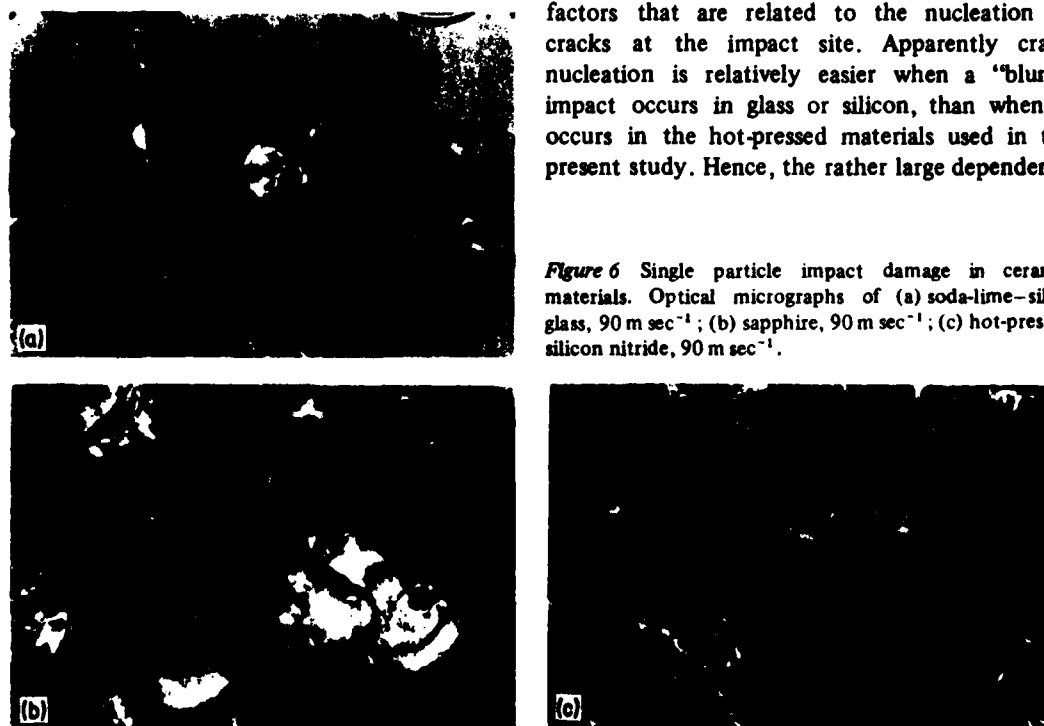


Figure 6 Single particle impact damage in ceramic materials. Optical micrographs of (a) soda-lime-silica glass,  $90 \text{ m sec}^{-1}$ ; (b) sapphire,  $90 \text{ m sec}^{-1}$ ; (c) hot-pressed silicon nitride,  $90 \text{ m sec}^{-1}$ .

of erosion rate on  $K_c$  and  $H$  reported in this paper can be attributed in part to statistical effects of particle orientation during erosion and the ease with which cracks nucleate in the target surface.

A second possible explanation for the observation of a larger than expected dependence of erosion rate on  $K_c$  and  $H$  has to do with the geometry of the cracks that form during the erosion process. The theories that have been proposed to explain erosion assume that cracks propagate from the impact site in a self-similar fashion, i.e. the cracks formed during impact are geometrically similar. Once nucleated, the cracks are assumed to propagate to the target surface. Thus, material is removed from the target by each impact. In contrast to these expectations, microscopic examination of the target surface indicates that the effectiveness of material removal from the target seems to depend on the fracture toughness of the target. Thus for the hot-pressed materials used in this study, cracks are often observed to arrest within the solid Fig. 7b and c so that cracking during impact does not result in material loss. A second or third impact in the vicinity of the

primary impact site is needed for material to be removed from the target. In contrast to this behaviour, complete chipping from the primary impact site is a more frequent occurrence for the more brittle materials such as silicon or glass (Fig. 7a). Thus, as the fracture toughness of the material increases, the efficiency of material removal per impact event is less than predicted theoretically, and the effect of  $K_c$  on the erosion rate is greater than predicted theoretically.

Before turning from the subject of microstructure, it is worth commenting on the erosion results obtained for aluminium oxide and sapphire. As can be seen from Fig. 2, the erosion rates of sapphire and sintered aluminium oxide are approximately three times that of the hot-pressed aluminium oxide. The difference in behaviour of the two polycrystalline materials is attributable to the difference in grain size of the two materials. The grain size, 3 to 4  $\mu\text{m}$ , of the hot-pressed material was considerably smaller than the size of the lateral cracks that were formed upon impact. As a consequence, lateral cracks interact with many grains during propagation, and the effective value of  $K_c$  resisting the growth of lateral cracks is that typical of polycrystalline aluminium oxide,  $\sim 4 \text{ MPam}^{1/2}$ . By contrast, lateral cracks formed in the sintered aluminium oxide, grain size  $\sim 30 \mu\text{m}$ , are usually contained within a single grain, and the effective  $K_c$  resisting crack growth is more typical of values obtained from single crystal fracture measurements,  $\sim 2 \text{ MPam}^{1/2}$ .

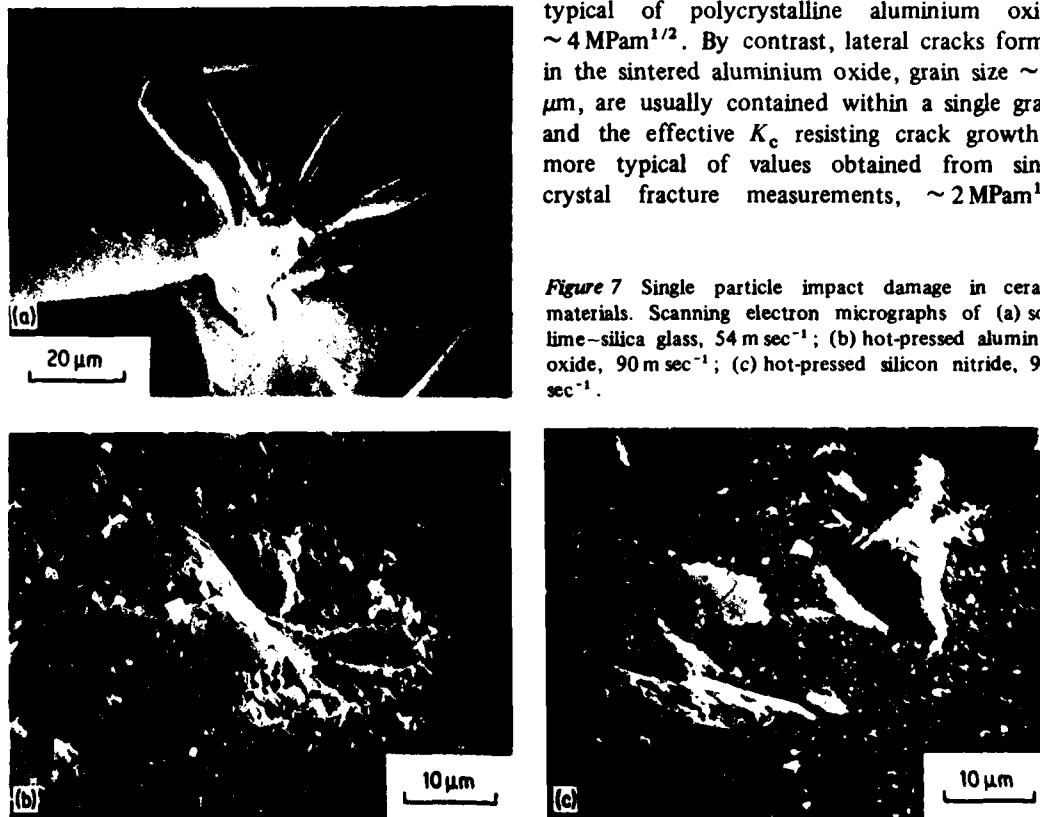


Figure 7 Single particle impact damage in ceramic materials. Scanning electron micrographs of (a) soda-lime-silica glass,  $54 \text{ m sec}^{-1}$ ; (b) hot-pressed aluminium oxide,  $90 \text{ m sec}^{-1}$ ; (c) hot-pressed silicon nitride,  $90 \text{ m sec}^{-1}$ .

Using Equation 9, the erosion rate for the large grain aluminium oxide should be approximately 3.7 times that obtained for the fine grained aluminium oxide. In Fig. 2, the erosion rate for the sintered aluminium oxide is approximately 3.3 times that of the hot-pressed material, which is close to the expected value. The fact that the erosion rate of the sintered aluminium oxide is close to that obtained for sapphire lends further support for this interpretation of the data.

#### 4.5. Erosion at elevated temperatures

As can be seen by comparing Figs. 3 and 4 with Fig. 2, the temperatures employed in the present study have a marginal effect on the rate of erosion. This finding is consistent with that reported earlier by the authors from a more limited set of data collected on some of the same materials studied in this paper [7]. Since dislocation mobility is enhanced by increasing the temperature, it was expected that both the hardness and fracture toughness, and hence the erosion rate, would be modified by increasing the temperature. Indeed, when loads are applied slowly, both the hardness and toughness of ceramic materials are strongly dependent on temperature [19, 26, 29, 42, 43]. The fact that significant changes in the erosion behaviour are not observed at elevated temperatures suggests that for conditions of dynamic loading, both the hardness and the toughness are invariant with temperature. This supposition is supported by dynamic toughness measurements on hot-pressed silicon nitride [44, 45], and by the fact that cracks are observed to form in soda-lime-silica glass at temperatures above the softening point of this glass [46, 47].

Although temperature does not play a dominant role in the erosion of ceramics under the conditions used in the paper, minor differences between low and elevated temperature behaviour can be attributed to plastic flow. Because lateral cracks form after the impact event and are driven by residual stresses at the impact site, relaxation of those stresses or modification of the resistance of the target to crack growth as a result of plastic deformation can alter the size of chips that are formed after impact. Such effects are feasible when the relaxation time of the material for plastic flow is less than the time required for the lateral cracks to complete their growth. In an earlier study on soda-lime-silica glass at 500°C, the temperature dependence of the erosion rate was attributed to

such plastic relaxation [46]. In the present study, the small differences between low and elevated temperature behaviour may also be attributable to the same types of processes.

#### Acknowledgements

The authors gratefully acknowledge the support of the Office of Naval Research, Metallurgy and Ceramics Program. Helpful discussions with B. R. Lawn are also gratefully acknowledged.

#### Appendix A:

##### Dimensionless erosion equation

This Appendix is written for those readers who are unfamiliar with the technique of dimensional analysis. A concise description of the technique can be found from Kay and Nedderman [48]. The procedure outlined in this reference is followed here.

Starting with Equation 6, we assume that the wear rate can be expressed as a power series expansion of the parameters  $v_0$ ,  $R$ ,  $\rho$ ,  $K_c$  and  $H$ :

$$W = \sum_i \alpha_i (v_0^{a_i} R^{b_i} \rho^{c_i} K_c^{d_i} H^{e_i}) \quad (A1)$$

$\alpha_i$  being a dimensionless coefficient for each term of the series. The dimensions of each term in the expansion must equal the dimensions of  $W$  in order for Equation A1 to be dimensionally consistent.

When the dimensions are substituted for the parameters in Equation A1, each term in the expansion must have the following dimensional form:

$$L^3 = (L/T)^{a_i} L^{b_i} (M/L^3)^{c_i} (M/T^2 L^{1/2})^{d_i} (M/T^2 L)^{e_i} \quad (A2)$$

where  $L$ ,  $T$ , and  $M$  represent the dimensions of length, time, and mass.

Equating the exponents for each dimension we obtain three simultaneous equations in terms of the exponents  $a_i$ ,  $b_i$ ,  $c_i$ ,  $d_i$ , and  $e_i$ . If two of the unknowns are selected as independent variables, the other unknowns can be expressed in terms of these two variables. For example, if  $c_i$  and  $d_i$  are selected then the following equations are obtained for  $a_i$ ,  $b_i$ , and  $e_i$ :

$$\begin{aligned} a_i &= -3 - 2c_i \\ b_i &= 3 - d_i/2 \\ e_i &= -c_i - d_i \end{aligned} \quad (A3)$$

If these are substituted into Equation A1, the

following expression is obtained for the wear rate  $W$ :

$$W/R^3 = \sum_i \alpha_i (v^2 \rho / H)^{c_i} (K_c^2 / RH^2)^{d_i / 2} \quad (\text{A4})$$

Since the two theories developed to explain erosion are power functions of the variables given in Equation A4, only one term in the series need be retained in order to compare the dimensional analysis with the theoretical expressions given by Equations 4 and 5. Hence, the following relation is obtained for the erosion rate:

$$W/R^3 = A (K_c^2 / RH^2)^a (\rho v^2 / H)^b \quad (\text{A5})$$

where  $A$  is a dimensionless constant and the exponents of Equation A4 have been written as  $a$  and  $b$ . Equation A5 is identical to Equation 7 of the text. As noted earlier, the undetermined constants  $a$  and  $b$  are evaluated by an empirical fit of erosion data.

Equation A5 is not a unique dimensionless representation of the parameters that control erosion. For example, if  $b_1$  and  $c_1$  had been selected as the independent constants, then the following erosion equation would have been obtained

$$W(H/K_c)^6 = A'(v^2 \rho / H)^c (RH^2 / K_c^2)^b \quad (\text{A6})$$

Equations A5 and A6 can be shown to be equivalent by dividing both sides of the equation by  $(RH^2 / K_c^2)^3$ . By systematically solving for all possible combinations of the exponents in Equation A1, five variants of Equation A5 were found. These could all be reduced to Equation A5 by judicial manipulation (multiplying or dividing) of the dimensionless parameters  $K_c^2 / RH^2$  and  $\rho v^2 / H$ .

There is a certain arbitrariness in selecting one of the dimensionless equations for a comparison with the experimental data. We justify the selection of Equation A5 on the basis of its simple form and the ease with which the dimensionless variables  $K_c^2 / RH^2$  and  $\rho v^2 / H$  can be given physical interpretation. Furthermore, this arrangement of the variables in Equation A5 separates the variants used in the present study more effectively than the others, and permits us to compare the theoretical equations with the results of the dimensional analysis more readily. Regardless of which form of the dimensionless analysis is used, one can show that they are all equivalent, provided the error is minimized in the term containing the wear rate, i.e.  $W/R^3$ . This equivalence can be demonstrated by using the basic equations for a multiple regression analysis [41].

## Appendix B

TABLE IB Summary of erosion data

Material	Temperature (°C)	Particle velocity (m sec <sup>-1</sup> )	Erosion rate (mm <sup>3</sup> )
Hot-pressed Si <sub>3</sub> N <sub>4</sub>	25	94	7.4 × 10 <sup>-7</sup> (0.8)*
		73	4.0 × 10 <sup>-7</sup> (0.6)
		37	9.9 × 10 <sup>-8</sup> (2.6)
	500	125	1.8 × 10 <sup>-6</sup> (0.2)
		90	8.1 × 10 <sup>-7</sup> (2.0)
		54	2.2 × 10 <sup>-7</sup> (0.4)
	1000	125	2.5 × 10 <sup>-6</sup> (0.2)
		90	9.9 × 10 <sup>-7</sup> (0.5)
	Hot-pressed SiC	25	94
73			5.3 × 10 <sup>-7</sup> (0.2)
37			1.4 × 10 <sup>-7</sup> (0.3)
Hot-pressed Al <sub>2</sub> O <sub>3</sub>	25	94	1.1 × 10 <sup>-6</sup> (0.2)
		73	6.0 × 10 <sup>-7</sup> (0.6)
		37	1.3 × 10 <sup>-7</sup> (0.4)
	500	125	2.5 × 10 <sup>-6</sup> (0.1)
		100	1.5 × 10 <sup>-6</sup> (0.1)
		54	4.1 × 10 <sup>-7</sup> (0.1)
	1000	125	2.5 × 10 <sup>-6</sup> (0.1)
		81	8.7 × 10 <sup>-7</sup> (0.6)
		54	3.8 × 10 <sup>-7</sup> (0.4)

TABLE IB continued

Material	Temperature (°C)	Particle velocity (m sec <sup>-1</sup> )	Erosion rate (mm <sup>3</sup> )	
Sintered Al <sub>2</sub> O <sub>3</sub>	25	90	3.2 × 10 <sup>-6</sup> (0.4)	
		73	2.0 × 10 <sup>-6</sup> (0.1)	
		37	4.3 × 10 <sup>-7</sup> (1.3)	
	500	125	9.1 × 10 <sup>-6</sup> (1.0)	
		90	3.9 × 10 <sup>-6</sup> (1.1)	
		54	8.8 × 10 <sup>-7</sup> (3.6)	
Sintered Al <sub>2</sub> O <sub>3</sub>	1000	125	6.7 × 10 <sup>-6</sup> (2.1)	
		90	2.8 × 10 <sup>-6</sup> (0.7)	
		81	1.8 × 10 <sup>-6</sup> (0.6)	
		54	7.0 × 10 <sup>-7</sup> (2.5)	
Sapphire	25	94	4.6 × 10 <sup>-6</sup> (0.4)	
		54	1.2 × 10 <sup>-6</sup> (0.1)	
		37	5.5 × 10 <sup>-7</sup> (0.1)	
	500	125	9.1 × 10 <sup>-6</sup> (1.0)	
		90	3.9 × 10 <sup>-6</sup> (1.1)	
		54	8.8 × 10 <sup>-7</sup> (3.6)	
	1000	125	9.8 × 10 <sup>-6</sup> (0.7)	
		94	3.8 × 10 <sup>-6</sup> (0.3)	
		54	6.4 × 10 <sup>-7</sup> (0.6)	
Silicon	25	94	2.1 × 10 <sup>-5</sup> (0.1)	
		54	4.1 × 10 <sup>-6</sup> (0.3)	
		37	1.4 × 10 <sup>-6</sup> (0.1)	
	500	125	6.5 × 10 <sup>-5</sup> (0.7)	
		54	2.6 × 10 <sup>-6</sup> (0.2)	
		1000	125	7.7 × 10 <sup>-5</sup> (1.0)
	1000	54	4.6 × 10 <sup>-6</sup> (0.7)	
		25	94	7.3 × 10 <sup>-6</sup> (0.7)
			37	9.8 × 10 <sup>-6</sup> (0.2)
Fused Silica	25	94	2.3 × 10 <sup>-5</sup> (0.3)	
		37	1.6 × 10 <sup>-6</sup> (0.2)	
	500	125	6.0 × 10 <sup>-5</sup> (0.5)	
		54	4.7 × 10 <sup>-6</sup> (0.0)	
Soda-lime-silica glass	25	94	3.2 × 10 <sup>-5</sup> (0.7)	
		73	1.7 × 10 <sup>-5</sup> (0.4)	
		54	7.1 × 10 <sup>-6</sup> (0.7)	
		37	3.2 × 10 <sup>-6</sup> (0.7)	
	500	125	4.4 × 10 <sup>-5</sup> (1.2)	
		100	2.2 × 10 <sup>-5</sup> (0.6)	
		73	8.3 × 10 <sup>-6</sup> (0.4)	
		54	2.3 × 10 <sup>-6</sup> (0.5)	

\*The numbers in parentheses are the standard deviation of each fit. Two to ten erosion measurements were used to determine each erosion rate.

### References

1. A. G. EVANS, in "Treatise on Materials Science and Technology" Vol. 16, edited by C. M. Preece (Academic Press, New York, 1979) pp. 1-67.
2. A. W. RUFF and S. M. WIEDERHORN, *ibid.* pp. 69-126.
3. B. A. LAWN and T. R. WILSHAW, *J. Mater. Sci.* 10 (1975) 1049.
4. M. M. CHAUDHRI and S. M. WALLEY, *Phil. Mag.* A37 (1978) 153.
5. C. G. KNIGHT, M. V. SWAIN and M. M. CHAUDHRI, *J. Mater. Sci.* 12 (1977) 1573.
6. B. R. LAWN and D. B. MARSHALL, in "Fracture Mechanics of Ceramics" Vol. 3, edited by R. C. Bradt, D. P. H. Hasselman, and F. F. Lange (Plenum Press, New York, 1978) pp. 205-229.
7. B. J. HOCKEY, S. M. WIEDERHORN and H. JOHNSON, *ibid.* pp. 379-402.
8. M. M. CHAUDHRI and P. A. BROPHY, *J. Mater. Sci.* 15 (1980) 345.
9. A. G. EVANS and T. R. WILSHAW, *ibid.* 12 (1977) 97.

10. A. G. EVANS, M. E. GULDEN and M. E. ROSENBLATT, *Proc. Roy. Soc. London Ser. A* **361** (1978) 343.
11. B. J. HOCKEY and B. R. LAWN, *J. Mater. Sci.* **10** (1975) 1275.
12. B. J. HOCKEY and S. M. WIEDERHORN, in "Proceedings of the 5th International Conference on Erosion by Liquid and Solid Impact" (Cavendish Laboratories, University of Cambridge, 1979) pp. 26-1-26-10.
13. B. R. LAWN, B. J. HOCKEY and S. M. WIEDERHORN, *J. Mater. Sci.* **15** (1980) 207.
14. B. R. LAWN and E. R. FULLER, *ibid.* **10** (1975) 2016.
15. S. M. WIEDERHORN and B. R. LAWN, *J. Amer. Ceram. Soc.* **62** (1979) 66.
16. M. E. GULDEN, *ibid.* **64** (1981) C59.
17. M. L. TORTÉ, R. A. ALLIEGRO, D. W. RICHERSON, M. E. WASHBURN and G. Q. WEAVER, *Proc. Brit. Ceram. Soc.* **22** (1973) 125.
18. R. W. RICE, S. W. FREIMAN and P. F. BECKER, *ibid.* **64** (1981) 345.
19. A. G. EVANS and S. M. WIEDERHORN, *J. Mater. Sci.* **9** (1974) 373.
20. W. S. COBLENTZ, *J. Amer. Ceram. Soc.* **58** (1975) 530.
21. J. L. CHERMANT, R. MOUSSA and F. OSTERSTOCK, *Rev. Int. Hautes Temp. Réfract.* **18** (1981) 5.
22. J. F. LYNCH, C. G. RUDERER and W. H. DUCKWORTH, "Engineering Properties of Selected Ceramic Materials" (American Ceramic Society, Columbus, Ohio, 1966).
23. L. M. BARKER, in "Fracture Mechanics of Ceramics" Vol. 3, edited by R. C. Bradt, D. P. H. Hasselman and F. F. Lange (Plenum Press, New York, 1978), pp. 483-494.
24. S. M. WIEDERHORN, B. J. HOCKEY and D. E. ROBERTS, *Phil. Mag.* **28** (1973) 783.
25. R. J. JACCODINE, *J. Electrochem. Soc.* **110** (1963) 524.
26. C. ST. JOHN, *Phil. Mag.* **32** (1975) 1193.
27. J. R. HUTCHINS III, and R. V. HARRINGTON, in "Kirk-Othmer Encyclopedia of Chemical Technology", edited by A. Standen (John Wiley and Sons, New York, 1966) pp. 533-604.
28. S. M. WIEDERHORN, *J. Amer. Ceram. Soc.* **52** (1969) 99.
29. J. H. WESTBROOK, *Rev. Hautes Temp. Réfract.* **t. 3** (1966) 47.
30. S. M. WIEDERHORN and D. E. ROBERTS, *Bull. Amer. Ceram. Soc.* **55** (1976) 185.
31. A. W. RUFF and L. K. IVES, *Wear* **35** (1975) 195.
32. R. J. FIELDS Jr, B. J. HOCKEY and S. M. WIEDERHORN, to be published.
33. G. L. SHELDON and I. FINNIE, *J. Eng. Ind., Trans. ASME*, **88** (1966) 393.
34. G. A. SARGENT, P. K. MEHROTRA and H. CONRAD, in "Erosion: Prevention and Useful Applications", ASTM STP 664, edited by W. F. Adler, (American Society of Testing and Materials Philadelphia, PA, 1979) pp. 77-100.
35. M. E. GULDEN, *ibid.* pp. 101-122.
36. R. O. SCATTERGOOD and J. L. ROUTBORT, *Wear* **67** (1981) 227.
37. J. L. ROUTBORT, R. O. SCATTERGOOD and P. A. L. TURNER, *ibid.* **59** (1980) 363.
38. J. L. ROUTBORT and R. O. SCATTERGOOD, *J. Amer. Ceram. Soc.* **63** (1980) 593.
39. P. W. BRIDGMAN, "Dimensional Analysis", (Yale University Press, New Haven, Conn., 1922).
40. B. R. LAWN, A. G. EVANS and D. B. MARSHALL, *J. Amer. Ceram. Soc.* **63** (1980) 574.
41. O. L. DAVIES, "Statistical Methods in Research and Production", (Oliver and Boyd, London, 1957).
42. A. G. ATKINS, in "The Science of Hardness Testing and its Research Applications", edited by J. H. Westbrook and H. Conrad (American Society for Metals, Metals Park, Ohio, 1973) pp. 223-240.
43. T. N. LOLADGE, G. V. BOKUCHAVA and G. E. DAVIDOVA, *ibid.* pp. 251-257.
44. M. G. MENDIRATTA, J. WIMMER and J. BRANSKY, *J. Mater. Sci.* **12** (1977) 212.
45. S. T. GONAZY and D. L. JOHNSON, in "Fracture Mechanics of Ceramics" Vol. 3, edited by R. C. Bradt, D. P. H. Hasselman and F. F. Lange. (Plenum Press, New York, 1978) pp. 495-506.
46. S. M. WIEDERHORN and B. J. HOCKEY, *J. Noncryst. Solids* **38** and **39** (1980) 433.
47. H. P. KIRCHNER and R. M. GRUVER, in "Fracture Mechanics of ceramics", Vol. 3, edited by R. C. Bradt, D. P. H. Hasselman and F. F. Lange (Plenum Press, New York, 1978) pp. 365-377.
48. J. M. KAY and R. M. NEDDERMAN, "An Introduction to Fluid Mechanics and Heat Transfer", 3rd edn (Cambridge University Press, Cambridge, 1974).

Received 18 March  
and accepted 19 July 1982

2. B.R. Lawn and S.M. Wiederhorn, "Contact Fracture in Brittle Materials," pp. 133-147 in *Contact Mechanics and Wear of Rail/Wheel Systems*, J. Halousek, R.V. Dukkipati and G.M.L. Gladwell, eds., University of Waterloo Press, 1982.

## CONTACT FRACTURE IN BRITTLE MATERIALS

B.R. Lawn and S.M. Wiederhorn  
Fracture and Deformation Division  
National Bureau of Standards  
Washington, D.C., U.S.A.

**ABSTRACT:** The nature of contact-induced surface damage in brittle materials, and the fracture mechanics principles used to describe this damage, are surveyed. The importance of understanding the elastic and plastic deformation processes which precede fracture is emphasized. Strength and erosive wear properties are intimately connected to the contact damage mechanics.

**RÉSUMÉ:** La nature de la détérioration par contact de la surface des matériaux fragiles et les principes de mécanique des fractures utilisés pour décrire cette détérioration sont rappelés. On souligne l'importance de la compréhension des processus de déformation élastique et plastique qui précèdent la fracture. La force et les propriétés d'érosion sont intimement liées aux mécanismes de dommage par contact.

### INTRODUCTION

The ubiquitous surface damage that characterises highly brittle materials, notably glasses and ceramics (i.e., solids with covalent/ionic bonding), is due to local stress concentrations that occur whenever contact is made with a small, hard object. Microfracture centers that seriously degrade the strength are often introduced by the processes used to finish the surfaces (e.g., machining), or by particle impingement incurred in subsequent handling and storage. Unless extreme precautions are taken to avoid all spurious contact events (e.g., as is done with the coating of freshly drawn optical fibres in dust-free atmospheres) such degradation is generally inevitable. Contact damage also holds the key to the erosive wear and abrasion properties of brittle materials. A proper understanding of the underlying mechanisms of deformation and fracture, using the controlled methods of "indentation fracture mechanics", has accordingly become a major research goal in the area of brittle design.

In the present paper the current state of this understanding is summarized. Our goal is not a comprehensive survey of the field: rather, we seek to draw attention to certain broad features of the brittle indentation problem that might be considered to bear, however indirectly, on the theme of this meeting. Reference is made to several review articles [1-4] for those who wish to pursue the subject in greater detail.

The outline of our presentation is as follows. First we define what we mean by a brittle solid. We then argue that indentation events can be classified into two main types, "blunt" or "sharp", according to whether the material response to fracture is essentially elastic or plastic. In normal loading the cracks are shown to have well-defined, penny-like geometries; superposition of a tangential loading component modifies these geometries significantly. Fracture mechanics relations are given for some of the more important of the crack geometries. Finally, the role of indentation fracture descriptions in formulating theories of strength and wear is discussed.

#### BRITTLE MATERIALS IN RELATION TO THE CONTACT PROBLEM

Ideally brittle materials are, by definition, essentially characterized by a completely elastic response up to the point of fracture. In certain instances stresses and strains close to the theoretical strength of the molecular structure can be sustained without detectable signs of permanent deformation. Coated silica glass fibers, for example, show complete recovery after undergoing tensile strains of up to 15%. The materials which fall most readily into this category are those with large components of covalent bonding, for which there exists a strong intrinsic resistance to shear-activated deformation processes [5].

However, even the most brittle of materials can, if subjected to sufficiently large constraining hydrostatic compressions to inhibit the onset of fracture, be deformed irreversibly [6]. (This statement is, of course, a self-evident truth to those concerned with the geomechanical behaviour of rocks.) Hardness indentations provide us with the simplest means of demonstrating this phenomenon; the stress field immediately beneath the contact area is intensely compressive, with a substantial component of superposed shear [7]. Thus residual impressions can be made on the surface of any material, including diamond, with a suitably penetrative indenter.

Whereas in metals the nature of the deformation processes which operate within the contact zone is reasonably well understood, in some of the more brittle materials the analogous processes remain obscure. It is clear from the magnitude of the contact pressures that the harder, covalent structures are being stressed to their theoretical limit. At this level the classical descriptions of slip by dislocation motion no longer strictly apply; instead it becomes more useful to consider the deformation modes in terms of an extended, cooperative breakdown of the structure. This is not to say that structures which undergo this kind of deformation are incapable of being "dislocated" by shear processes. Indeed, structural dislocations have been clearly identified in transmission electron microscopy observations by Hockey at indentation sites in a number of hard crystalline materials [8-10]. However, the configurations observed do not always correspond to normal crystallographic slip planes or directions. In fact, the recent identification of analogous shear processes in soda-lime glass [11] would appear to indicate that crystallographic considerations are no longer of primary importance in the constrained deformation of this class of solid.

A characteristic feature of the contact deformation zone in highly brittle materials is its strong confinement to the region immediately below the surface impression. There is no mechanism for relaxation of the "plastic" strains as there is in most metals, where extensive, long-range slip or twinning can usually occur without obstruction. Instead, these strains have to be accommodated elastically by the surrounding matrix. Consequently, high-intensity residual stress fields can develop, and these fields can exert a strong influence on subsequent mechanical response of the material.

A second characteristic feature of the contact process in brittle materials is the great ease with which microcracks initiate and propagate. In a covalent material like silicon, for instance, it is almost impossible to produce crack-free impressions, with even the most delicate of routine hardness testing machines. In this context it may be noted that a tensile stress component, however small in comparison to the hydrostatic compression within the deformation zone, is generally unavoidable in the matrix contact field [1].

#### BLUNT VERSUS SHARP CONTACT

The nature of the stress field in an indentation experiment depends strongly on the geometry of the contacting surfaces, as well as on the mechanical properties of the materials involved. We shall be working on the premise here that the indenter material is sufficiently "hard" relative to that of the test piece to be effectively rigid. It is then convenient to distinguish two extreme types of indentation field [1]: "blunt", in which the contact pressure increases monotonically with load such that the deformation prior to fracture is completely elastic; "sharp", in which the contact pressure is in excess of that required to produce irreversible deformation at all stages of loading. The intensity of the stress field in the former case is controlled by the elastic moduli, in the latter by a combination of the elastic moduli and the hardness.

#### *Blunt Contact*

The classical example of the blunt contact is the Hertzian stress problem, discussed at some length by others in this volume. Experimentally, the Hertzian stress field is most simply generated by pressing a sphere onto a semi-infinite solid. Solutions for the field are obtained from the basic equations of linear elasticity. Essentially, the normal stresses are all highly compressive in a drop-shaped zone immediately below the indenter, but become moderately tensile at and outside the contact circle. These tensile stresses are extremely inhomogeneous in this near-contact region, falling off dramatically along subsurface stress trajectories [1,12]. Remote from the contact zone the stress field tends asymptotically to the corresponding Boussinesq field for concentrated point loading [1,13].

At a critical load in the Hertzian contact a well-defined, cone-shaped crack "pops in" from the specimen surface. Figure 1 shows such a Hertzian fracture in glass.

The stresses at the surface trace prior to pop-in are generally well below the theoretical limiting strength of the material structure, indicating that initiation must occur from pre-present flaws. The crack first runs from the critical surface flaw into a shallow ring just outside the contact circle, then propagates downward into its characteristic cone geometry until sufficiently remote from the loading center, at which point it becomes highly stable.

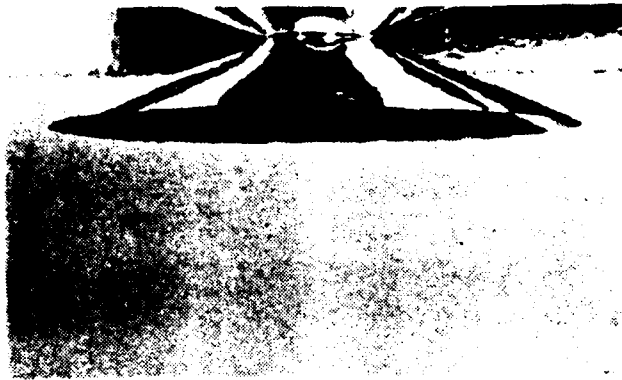


*Figure 1 - Cone Crack in Glass; Base Diameter 30 mm, Indentation Load 40 MN. After [15].*

The mechanics of formation of Hertzian cone cracks is complicated by the extreme inhomogeneity of the near-contact stress field through which the growth occurs. To ignore this inhomogeneity and assume that instability ensues when the surface stresses reach the tensile strength of the material is to overlook the essence of the general contact fracture phenomenon. In accordance with modern-day fracture mechanics procedure it is necessary to compute a "stress intensity factor", representing the driving force for the fracture, as an integral of actual stresses (weighted with an appropriate Green's function) over the prospective crack path. The first such analysis was carried out by Frank and Lawn [12], who showed that the critical load for cone-crack pop-in, under equilibrium conditions of fracture, is given by

$$P_c = A_1 K_c^2 r / E, \quad (1)$$

where  $r$  is the sphere radius,  $K_c$  is the critical stress intensity factor for crack extension (i.e., the material "toughness", characterizing the intrinsic resistance to fracture).  $E$  is Young's modulus and  $A_1$  is a dimensionless constant. This result provided the first analytical derivation of the long-standing empirical "law" of Auerbach, 1891,  $P_c \propto r$  [14]. Considerable interest has been shown in this law because the Hertzian equations for the surface stresses give  $\sigma \propto P/r^2$  so that, in combination with equation (1), we obtain  $\sigma_c \propto 1/r$ ; i.e., the simplistic concept of a critical stress criterion for fracture is clearly in violation. Note that this last expression implies the suppression of crack

initiation at small sphere radii - the possibility of inducing precursor plasticity thus becomes stronger for "sharper" indenters.

The size to which the cone crack grows, once initiated, is determined by the far-field conditions. Roesler [15], using a dimensional analysis argument, showed that the crack size increases with load according to  $c \propto P^{2/3}$ . A more detailed, fracture mechanics treatment [16] gives, at equilibrium,

$$P/c^{3/2} = A_2 K_c, \quad (P > P_c), \quad (2)$$

where  $A_2$  is another dimensionless constant.

It is interesting to note that neither of equations (1) and (2) is sensitive to the size of the critical flaw from which the cone crack initiates. This insensitivity is another characteristic of the general contact problem, although it is implicit in the derivation of the above expressions that there is always a sufficiently high density of surface flaws present to guarantee the initiation condition. It may also be noted that the formulations contain the toughness  $K_c$ , the definition of which strictly implies a configuration of mechanical equilibrium (unstable in relation to equation (1), stable in equation (2)). In practice, brittle materials are susceptible to chemically-enhanced rate-dependent crack growth, particularly in the presence of atmospheric moisture, in which case equation (1) tends to overestimate the critical load and equation (2) to underestimate the crack size.

The mechanics of fracture are modified somewhat by the superposition of a tangential force component onto the normal loading configuration. Stress solutions for the case of complete slippage at a sliding contact interface have been described by Hamilton and Goodman [17]. The main effect of the tangential force is to enhance the tensile stresses at the trailing edge of the advancing sphere, thereby destroying the axial symmetry of the field. Consequently, the critical load for fracture is reduced, dramatically at the higher coefficients of friction, and the cracks form only partial (highly distorted) cones [18]. The modified field for a coefficient of friction 0.1 is shown in Figure 2, together with a micrograph for the corresponding conditions in a sliding friction test on a glass surface [19]. Formulations analogous to equations (1) and (2) for the sliding sphere have been attempted by several workers, but a strong sensitivity to starting assumptions in the analysis has led to considerable divergence in the various predictions, particularly in the critical load.

#### *Sharp Contact*

We alluded in the previous subsection to the increasing prospect of precursor inelastic deformation with diminishing indenter radius. In the limit of zero radius, e.g., as with an ideally sharp Vickers or Knoop pyramidal indenter, such deformation becomes unavoidable; a finite load cannot be supported by a point contact without exceeding the elastic limit. The stress field beneath the indenter is considerably more complex than

in its Hertzian elastic counterpart, and simplistic elastic/plastic models have to be devised to provide a necessary framework for fracture mechanics analysis. The simplest and most widely adopted of the models is that of the expanding internal cavity, in which a pressurized spherical volume (hardness impression) induces plasticity in an immediate annular surround volume (deformation zone), the whole being constrained in an infinite elastic matrix [20,21]. Despite clear shortcomings, e.g., failure to allow for stress relaxation at the specimen free surface and failure to match the Boussinesq point-force solution in the far field, models of this type are useful for their amenability to closed-form solution.

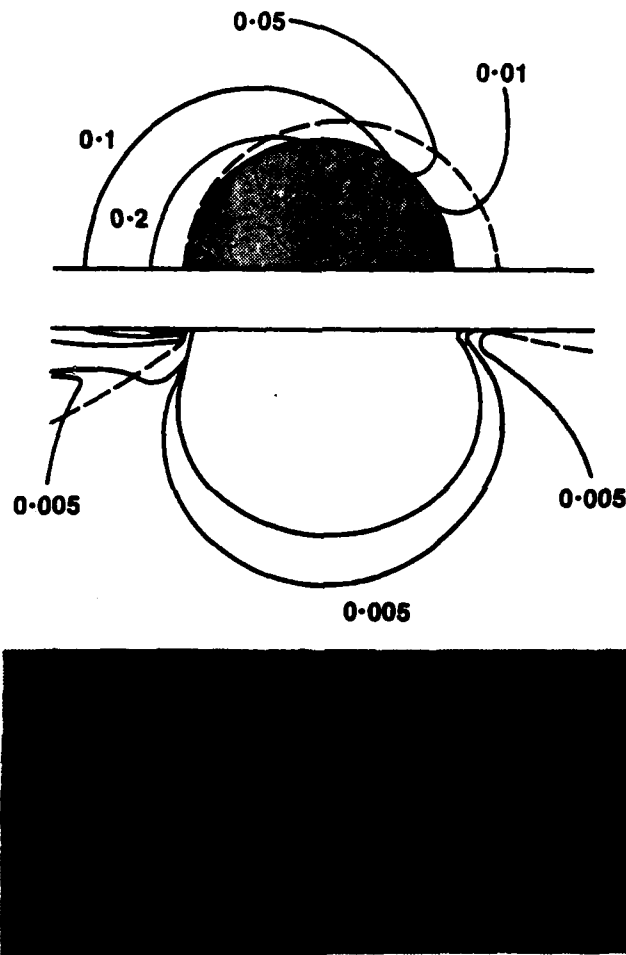


*Figure 2 - Sliding Contact Fracture Beneath Sphere, Friction Coefficient 0.1. Schematic half-surface and side views show contours of maximum tension (solid curves) and principal stress trajectories (dashed curves) about contact circle (shaded). After [18]. Micrograph shows partial cone tract on glass, width 25  $\mu$ m, produced by sphere of radius 1.5 mm at load 10 N. After [19].*

The fracture pattern produced in sharp indentation has some geometrical variants, but two basic crack types are generally distinguishable; median/radial, and lateral, cracks [13]. Figure 3 is an illustrative example, again in glass. It is found that the initiation of such cracks is accomplished with relative ease in highly brittle materials, even on surfaces of the greatest perfection, suggesting that the precursor deformation processes are capable of producing their own fracture nuclei [11]. Each median crack forms on a symmetry plane containing the contact axis and an impression diagonal, and leaves a characteristic radial trace on the indented surface; as seen in Figure 3, more than one crack of this type can be formed in a given contact, depending on the indenter geometry. Lateral cracks form in a saucer-like manner, starting from near the base of the deformation zone and spreading outward closely parallel to the specimen surface; in severe cases the laterals can extend to the surface, causing chipping. As with the Hertzian cones these cracks, once developed, are highly stable.



*Figure 3 - Median/Radial/Lateral Fracture System for Vickers Indentation on Glass; Radial Crack Diameter 1.3 mm, Load 100 N. Courtesy of B.J. Hockey.*

The conditions for the initiation of indentation cracks beneath sharp indenters have only recently been considered. Lawn and Evans [22] used a fracture mechanics procedure somewhat analogous to that in the earlier cone crack analysis [12], but with the

intensity of the stress field now determined by a load-invariant hardness  $H$ . In their scheme fracture occurs when the spatial extent of the field, as determined by the contact dimension, is sufficiently large to make available flaws within the deformation zone unstable. Accordingly, the critical load is found to be

$$P_c = A_3 (E/H) (K_c/H)^3 K_c, \quad (3)$$

where  $A_3$  is a dimensionless term involving the characteristic indenter half-angle. Whereas the analysis is acknowledged to be deficient in its ability to specify the absolute value of  $A_3$ , Equation (3) serves well as a basis for ranking materials. For example, comparison of a moderately hard steel with a typical silicate glass leads to a predicted ratio of  $\approx 10^3 - 10^4$  in  $P_c$  values, thus explaining the brittleness of the latter [7].

In considering the mechanics of well-developed median and lateral cracks we can take note of one geometrical feature common to all far-field indentation fracture configurations; their ultimate fronts tend to be circular, so they have the essential character of center-loaded penny cracks [16]. For the median cracks, which approximate to half-pennies centered on the point of contact, detailed analysis provides a relation between load  $P$  and crack radius  $c$ , [23]

$$P/c^{3/2} = A_4 (H/E)^{1/2} K_c, \quad (P > P_c)$$

in direct analogy to equation (2), with  $A_4$  again incorporating the indenter half-angle. However, if the final configuration of the median crack bears a strong underlying resemblance to that of its cone crack counterpart, its route to this configuration during the indentation cycle is of a totally different nature. For, in addition to the usual crack driving force associated with the reversible (elastic) component of the stress field, there is also a contribution from the irreversible (plastic) component, and it is the second of these components which dominates in the median crack evolution. Thus, much of the crack evolution occurs as the indenter is being unloaded, particularly along the radial traces in the near-surface region [23,24]. Indeed, in materials susceptible to moisture-enhanced crack growth, the radial crack traces can be observed to continue extending long after the indenter has been removed.

Derivation of a similar expression for lateral cracks is even less straightforward, owing to the added complication of the nearby specimen free surface. Whereas for the more penetrative median and cone cracks the free surface is unlikely to have a strong influence on the strain energy distributions which govern crack extension, the same is certainly not true of the highly compliant material portions immediately above the lateral plane. Thus, although the lateral system retains the penny-like character, it is more realistic to regard it in terms of a thin, circular disc of material built in at its circumference to a rigid matrix rather than in terms of the usual embedded configuration. Using the theory of elastic plates to determine the energetics of this system a result analogous to equation (4) can be derived [25], except that now the

relation between crack size and load is of the form  $c \propto P^{5/8}$  and the dependence on material parameters is somewhat more complex. Again, the bulk of the crack growth takes place during indenter withdrawal, re-emphasising the crucial role of residual stresses when inelastic deformation accompanies fracture.

When a sharp indenter is translated across the surface of a brittle material it leaves a scratch track. Again, the introduction of a frictional force, this time determined by a "ploughing" process, enhances the fracture development [26]. In environment-sensitive materials rate variables, such as scratch velocity, become a factor. In accordance with the arguments leading to equation (3) it is found that "light" loads tend to produce smooth scratches, "heavy" loads fragmented scratches. In the former case the action is one of "polishing", in the latter of "abrasion" [1]. Figure 4 shows an example of a scratch made just above the threshold load in glass. (Note that a cursory examination of the surface in this case would create the false impression of a purely plastic contact event.) Comparison of Figure 4 with Figure 3 shows that the sliding motion tends to suppress one set of median cracks, thus producing an essentially linear flaw. At excessively high loads extensive chipping occurs along the length of the scratch as the laterals turn upward to intersect the surface. This can lead to physical removal of the deformation zone, and thereby of the source of the residual driving force on the subsurface median crack.

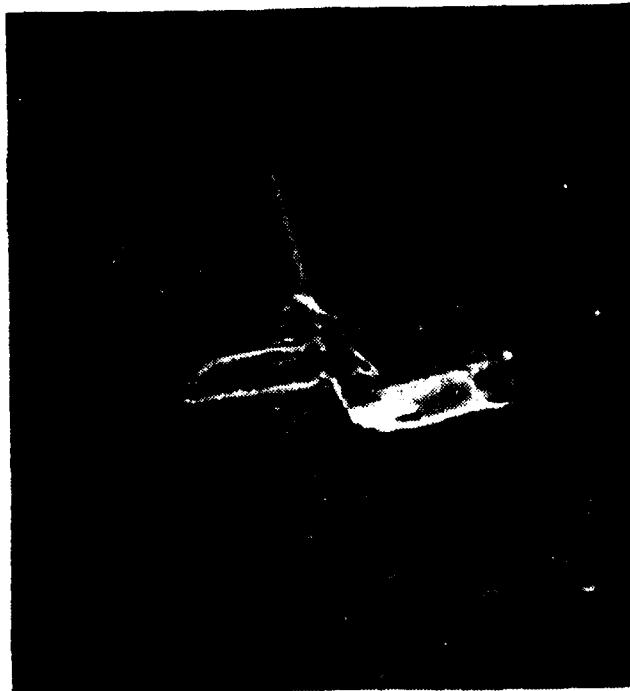


*Figure 4 - Scratch on Glass,  $\approx 10 \mu\text{m}$  wide, made by sliding Vickers Indenter at load 1 N. After [26].*

## PRACTICAL APPLICATIONS

Extensive experimental confirmation of the preceding theoretical formulations has provided us with a sound foundation for modelling various practical processes in brittle glasses and ceramics. We shall focus our attention on two of the more important of these processes, strength degradation and erosive wear. In the first case it is the penetrative cone or median crack which is the governing element; in the second case the lateral system dominates.

### *Strength Degradation*

The strength of a brittle material is controlled by the size of the largest flaw in the surface or bulk. In many cases this dominant flaw results from a well-characterized contact event, e.g., from machining during fabrication or particle impact in service. Failure then becomes a function of the contact variables, which can often be accurately specified. This accuracy can be optimized by deliberately introducing controlled indentation cracks into prospective test pieces. Apart from circumventing many uncertainties associated with the usual statistical approach to the strength of materials with unclassified flaws, this course opens up many avenues to systematic materials evaluation [4]. Moreover, by observing how "macroscopic" contact-induced cracks respond under an applied tensile stress we can gain valuable physical insight into the nature of "microscopic" natural flaws which are generally undetectable.

As an example of the type of information that can be obtained from strength degradation studies we present results from a ballistic impact study on glass surfaces using steel spheres, Figure 5 [27]. The micrograph shows the damage incurred at one specified impact velocity, and the graph shows how the remaining strength varies systematically with this velocity. The solid curve through the data points is a prediction from the conventional strength formula for spontaneous failure from flaws of characteristic size  $c_0$ ,

$$S = K_c / Yc_0^{1/2}$$

where  $Y$  is a geometrical constant close to unity;  $c_0$  is evaluated in accordance with equations (1) and (2) for blunt indenters, using the Hertzian contact theory to eliminate load as an unknown in favour of velocity [27]. We note that no degradation occurs in Figure 5 below the threshold velocity for cone crack pop in, at which point the strength drops abruptly; beyond the threshold the strength falls off steadily with increasing velocity.

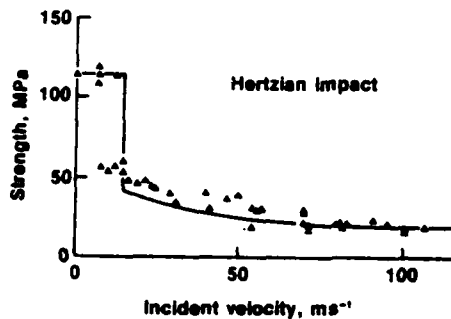


Figure 5 - Strength Degradation of Glass Impacted by Spheres. Micrograph shows surface damage after impact with 35-mesh glass beads; diameter of cone crack surface trace 400  $\mu\text{m}$ , incident velocity 100  $\text{ms}^{-1}$ . Graph shows remaining strength as function of impact velocity with steel spheres, diameter 0.8 mm. After [27].

The strength behaviour of materials containing median flaws induced by sharp contact is more complicated, owing to the active role of residual stresses from the plastic enclave in post-contact crack growth [28]. As a result of a strong stabilizing influence of the residual component in the net driving force for fracture, the medians do not propagate spontaneously to failure in the manner of cone cracks, but rather undergo a precursor stage of growth from  $c_0$  to a critical size  $c_m$  before attaining an instability configuration. Some data taken from direct observations of radial crack growth during application of a tensile stress to Vickers indented glass test pieces is plotted in Figure 6. The critical applied stress  $\sigma_m$  defines a new strength level [28]

$$S = K_C / 2Yc_m^{1/2}, \quad (6)$$

which is always less than the evaluation from equation (5). Hence the presence of residual stresses has a clearly detrimental effect on the structural integrity of materials. It can be shown from the fracture mechanics that  $c_m \propto (P/K_C)^{2/3}$ , independent of the initial flaw size  $c_0$ , so that control of strength can be exercised via the indentation load  $P$ .

It is this feature which establishes equation (6) as an attractive base formula for the accurate determination of material fracture parameters from strength data [4].

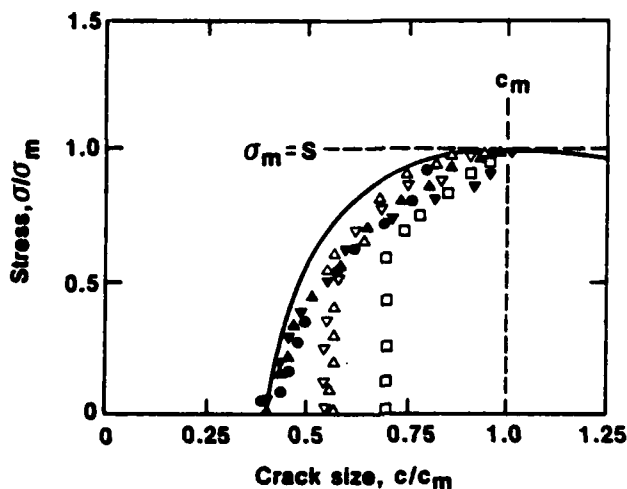


Figure 6 - Stable Crack Extension in Vickers-Indented Glass Prior to Failure in Tensile Loading. Stress and crack size normalized to coordinate values at maximum in curve. Closed symbols denote specimens confined to inert environment prior to failure test to suppress post-indentation crack creep, open symbols denote corrosive (moist) environment. Note failure conditions insensitive to initial crack size. Courtesy of D.B. Marshall.

One area of particularly intense recent interest in relation to the issue of materials evaluation is that of "fatigue", which in the ceramics testing fraternity is taken to mean strength loss due to environmentally-assisted crack growth during a static or monotonically increasing applied tensile stress. The introduction of indentation flaws into fatigue test pieces allows for determination of appropriate rate parameters for the underlying crack growth process, with unprecedented experimental simplicity and specimen economy [29,30]. More significantly in the present context, however, it highlights the dramatic increase in susceptibility to fatigue effects that flaws exhibit when residual stresses are present. For instance, by annealing out such stresses from Vickers-indented glass test pieces the lifetime at a prescribed applied load is extended by some three orders of magnitude [31]. There are important implications here in establishing design criteria for brittle materials, especially in view of a growing conviction that many "natural" flaws may be more closely simulated by indentation cracks in their "as-produced" rather than "annealed" state.

At the time of writing, studies of strength degradation for indenters subject to translational motion have only just begun. Early indications are that the linear flaws produced in this type of contact are likely to be even more strongly influenced by residual stress effects than are the simple point-contact flaws described above.

## Erosive Wear

The fracture mechanics relations derived earlier can also be used to develop models for erosive wear, where one seeks to inhibit cracking, and for machining, where one seeks to promote cracking. Sharp indenters are most effective in such material removal processes because of the relative ease with which lateral cracks form intersections with the free surface. Accordingly, most treatments of erosive wear and machining damage have concentrated on this contact mode. We shall consider just one practical example, that of erosion by normally incident sharp particles, to illustrate the modelling procedure.

The basic starting equation for the formulation defines the approximate amount of material removed in a single impact event,

$$\Delta V = \pi c^2 d, \quad (7)$$

where  $c$  is the radius and  $d$  the depth of the subsurface lateral crack. The crack radius is estimated from the lateral crack analogue of equation (4), and the depth from the penetration of the deformation zone. An appropriate impulse relation is once again required to eliminate contact load in favour of incident velocity. Summation over all impacts, assuming zero interaction between neighbours, leads to a functional relation (usually in power-law form) for the total volume removal rate in terms of the particle kinetic energy and material parameters. Unfortunately, the final expression obtained is extremely sensitive to minor details in the analysis (note equation (7) involves the cube of a linear dimension, whereas the strength formulae of equations (5) and (6) involve only the square root), and erosive data are notorious for their scatter, the result of which is an accumulation of slightly different, experimentally indistinguishable theories [32,33]. Thus the complexity of the erosion process admits only a partial theoretical account of experimental behaviour.

## ACKNOWLEDGEMENT

This project was supported by the Office of Naval Research, Metallurgy and Ceramics Program.

## REFERENCES

- [1] LAWN, B.R. and WILSHAW, T.R., "Indentation Fracture: Principles and Applications", *J. Mater. Sci.*, Vol. 10, 1975, p. 1049.
- [2] LAWN, B.R. and MARSHALL, D.B., "Indentation Fracture and Strength Degradation of Ceramics", *Fracture Mechanics of Ceramics*, Edited by R.C. Bradt, D.P.H. Hasselman and F.F. Lange, Plenum Press, New York, Vol. 3, 1978, p. 205.
- [3] LAWN, B.R. and MARSHALL, D.B., "Mechanisms of Microcontact Fracture in Brittle Solids", *Lithic Use-Wear Analysis*, Edited by B. Hayden, Academic Press, New York, 1979, p. 63.

- [4] LAWN, B.R., "The Indentation Crack as a Model Surface Flaw", *Fracture Mechanics of Ceramics*, Edited by R.C. Bradt, D.P.H. Hasselman, F.F. Lange and A.G. Evans, Plenum Press, New York, 1982, in press.
- [5] KELLY, A., *Strong Solids*, Clarendon, Oxford, 1966, Chapters 1 and 3.
- [6] BRIDGEMAN, P.W., *The Physics of High Pressures*, G. Bell, London, 1949.
- [7] LAWN, B.R. and MARSHALL, D.B., "Hardness, Toughness and Brittleness: An Indentation Analysis", *J. Amer. Ceram. Soc.*, Vol. 62, 1979, p. 347.
- [8] HOCKEY, B.J., "Plastic Deformation of Aluminum Oxide by Indentation and Abrasion", *J. Amer. Ceram. Soc.*, Vol. 54, 1971, p. 223.
- [9] HOCKEY, B.J. and LAWN, B.R., "Electron Microscopy of Microcracking About Indentations in Aluminum Oxide and Silicon Carbide", *J. Mater. Sci.*, Vol. 10, 1975, p. 1275.
- [10] LAWN, B.R., HOCKEY, B.J. and WIEDERHORN, S.M., "Atomically Sharp Cracks: An Electron Microscopy Study", *J. Mater. Sci.*, Vol. 15, 1970, p. 1207.
- [11] HAGAN, J.T., "Shear Deformation Under Pyramidal Indentations in Soda-Lime Glass", *J. Mater. Sci.*, Vol. 15, 1980, p. 1417.
- [12] FRANK, F.C. and LAWN, B.R., "On the Theory of Hertzian Fracture", *Proc. Roy. Soc. London*, Vol. A299, 1967, p. 291.
- [13] LAWN, B.R. and SWAIN, M.V., "Microfracture Beneath Point Indentations in Brittle Solids", *J. Mater. Sci.*, Vol. 10, 1975, p. 113.
- [14] AUERBACH, F., "Measurement of Hardness", *Ann. Phys. Chem.*, Vol. 43, 1891, p. 61.
- [15] ROESLER, F.C., "Brittle Fractures Near Equilibrium", *Proc. Phys. Soc. London*, Vol. B69, 1956, p. 981.
- [16] LAWN, B.R. and FULLER, E.R., "Equilibrium Penny-Like Cracks in Indentation Fracture", *J. Mater. Sci.*, Vol. 10, 1975, p. 2016.
- [17] HAMILTON, G.M. and GOODMAN, L.E., "The Stress Field Created by a Circular Sliding Contact", *J. Appl. Mech.*, Vol. 33, 1966, p. 371.
- [18] LAWN, B.R., "Partial Cone Crack Formation in a Brittle Material Loaded with a Sliding Spherical Indenter", *Proc. Roy. Soc. London*, Vol. A299, 1967, p. 307.
- [19] CRIMES, G.M., *Ph. D. Thesis*, University of Sussex, England, 1973.
- [20] HILL, R., *The Mathematical Theory of Plasticity*, Oxford University Press, London, 1950, Chapter 5.
- [21] JOHNSON, K.L., "The Correlation of Indentation Experiments", *J. Mech. Phys. Solids*, Vol. 18, 1970, p. 115.
- [22] LAWN, B.R. and EVANS, A.G., "A Model for Crack Initiation in Elastic/Plastic Indentation Fields", *J. Mater. Sci.*, Vol. 12, 1977, p. 2195.
- [23] LAWN, B.R., EVANS, A.G. and MARSHALL, D.B., "Elastic/Plastic Indentation Damage in Ceramics: The Median/Radial Crack System", *J. Amer. Ceram. Soc.*, Vol. 63, 1980, p. 574.
- [24] MARSHALL, D.B. and LAWN, B.R., "Residual Stress Effects in Sharp Contact Cracking: I. Indentation Fracture Mechanics", *J. Mater. Sci.*, Vol. 14, 1979, p. 2001.
- [25] MARSHALL, D.B., LAWN, B.R. and EVANS, A.G., "Elastic/Plastic Indentation Damage in Ceramics: The Lateral Crack System", *J. Amer. Ceram. Soc.*, in press.
- [26] SWAIN, M.V., "Microfracture about Scratches in Brittle Solids", *Proc. Roy. Soc. London*, Vol. A366, 1979, p. 575.
- [27] WIEDERHORN, S.M. and LAWN, B.R., "Strength Degradation of Glass Resulting from Impact with Spheres", *J. Amer. Ceram. Soc.*, Vol. 60, 1977, p. 451.
- [28] MARSHALL, D.B., LAWN, B.R. and CHANTIKUL, P., "Residual Stress Effects in Sharp Contact Cracking: II. Strength Degradation", *J. Mater. Sci.*, Vol. 14, 1979, p. 2225.
- [29] LAWN, B.R., MARSHALL, D.B., ANSTIS, G.R. and DABBS, T.P., "Fatigue Analysis of Brittle Materials Using Indentation Flaws: I. General Theory", *J. Mater. Sci.*, Vol. 16, 1981, p. 2846.

- [30] COOK, R.F., LAWN, B.R. and ANSTIS, G.R., "Fatigue Analysis of Brittle Materials Using Indentation Flaws: II. Case Study on a Glass Ceramic", *J. Mater. Sci.*, in press.
- [31] CHANTIKUL, P., LAWN, B.R. and MARSHALL, D.B., "Micromechanics of Flaw Growth in Static Fatigue: Influence of Residual Contact Stresses", *J. Amer. Ceram. Soc.*, Vol. 64, 1981, p. 322.
- [32] RUFF, A.W. and WIEDERHORN, S.M., "Erosion by Solid Particle Impact", *Treatise on Materials Science and Technology: Erosion*, edited by C.M. Preece, Academic Press, New York, Vol. 16, 1979, p. 69.
- [33] WIEDERHORN, S.M. and HOCKEY, B.J., "Effect of Material Parameters on the Erosion Resistance of Brittle Materials", *J. Mater. Sci.*, in press.

3. C.J. Fairbanks, R.S. Polvani, S.M. Wiederhorn, B.J. Hockey and B.R. Lawn, "Rate Effects in Hardness," J. Mat. Sci. Letters, 1, 391-393 (1982).

## Rate effects in hardness

C. J. FAIRBANKS\*, R. S. POLVANI, S. M. WIEDERHORN, B. J. HOCKEY,  
B. R. LAWN

*Fracture and Deformation Division, National Bureau of Standards, Washington, DC 20234, USA*

Hardness testing is gaining popularity as a scientific tool for evaluating the deformation properties of materials [1]. Its simplicity and economy are particularly well suited to systematic investigation of the many variables which are manifest in the general deformation response of any given material. Time is one of the more significant of these variables, for it contains the key to the kinetics and dynamics of material behaviour at the micro-mechanical level. Such rate effects could be an important design consideration where hardness values are taken as a basis for predicting strength, erosion and wear characteristics of solids.

Reports in the literature of rate dependencies in hardness measurements are sparse. The earliest studies, on metals, showed effects which appeared to reflect general creep properties; thus whereas indium showed substantial decreases in hardness with increasing indentation time [2] metals with higher melting points apparently did not, unless the test temperature was raised to a sufficiently high level [3]. Similar indentation creep phenomena were later reported for some ionic solids [4, 5]. A study on a wide range of other nonmetallic solids showed somewhat analogous behaviour for low-load indentations ( $< 1$  N) [6], but the effect disappeared at higher loads; this led the authors of that study to conclude that they were observing a spurious manifestation of surface-adsorbed water. Gunasekera and Holloway [7], in perhaps the most detailed investigation of this kind, found strong rate sensitivities in the hardness of silicate glass, depending on both the environment and the state of the surface; the loads used in their study were sufficiently large (1 to 5 N) for these workers to convince themselves they were not simply recording an artifact of either the experimental procedure or the material.

The results to be described in the present paper represent preliminary findings of a proposed

comprehensive programme to investigate time-dependent mechanical properties of selected engineering materials. Specifically, we report on the hardness response of a copper single crystal [(110) surface orientation], polycrystalline tungsten (grain size  $\approx 1 \mu\text{m}$ ) and crown silicate glass (thermally tempered, to minimize the incidence of radial cracking at the indentation corners); these three candidates were chosen simply to embrace a range of material types.

The hardness testing apparatus used in the study represents a modification of that described by Gunasekera and Holloway [7]. An electromagnetic transducer is used to drive the indenter arm vertically downward onto the surface of a rigidly mounted specimen. The compliance of the mechanical support for the coil in this system is sufficiently small that the load delivered is determined exclusively by the electrical input to the transducer, independent of any indenter movement relative to the specimen surface. In our experiments a sinusoidal signal is used to minimize complications due to inertial effects. The indenter is a standard Vickers diamond pyramid. The indentation load is monitored directly by means of a piezoelectric or strain-gauge-instrumented cell, depending on whether the contact period is less than or greater than  $\approx 1$  sec. These cells are generally located immediately below the specimen (see below, however). The load-time pulses, along with the corresponding activation pulses from the sine-wave generator, are recorded on an oscilloscope. With this arrangement an accuracy of  $\approx 2\%$  in the load measurement is readily attainable. The indentations produced are then measured optically in the usual way, and the hardness evaluated from the averaged impression diagonals on a projected contact area basis.

Initial runs to test the performance of the above system soon revealed difficulties due to

\*Cooperative Education Program Student at Virginia Polytechnic Institute.

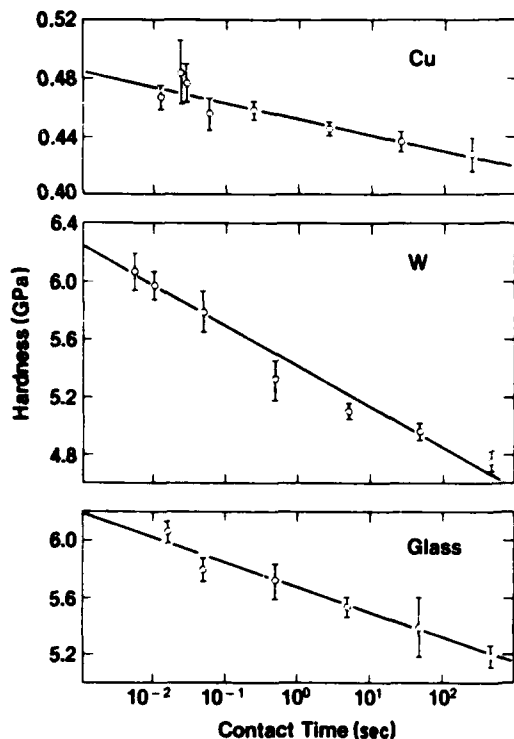


Figure 1 Vickers hardness as function of contact period for three materials. Solid lines are empirical fits to the data.

resonance effects at contact times much less than 10 msec. In this region the load pulse began to reduce in amplitude and to lag in phase relative to the input signal; spurious oscillations also became apparent. The inertia of the indenter drive system was certainly a contributing factor here, as could be demonstrated by removing the piezoelectric load cell from below the specimen and relocating it in the actual indenter arm; the recorded peak load, and thence the hardness evaluation, were much reduced by this interchange. We may note in passing that such artificially low readings could, if not properly accounted for, lead one to conclude that a given material is actually undergoing a rate-induced softening, e.g., due to localized adiabatic heating [8]. In any event, we avoid such potential ambiguities in interpretation here by including only data from indentations whose load pulses were entirely free of any resonance effects.

For the runs proper, indentations were made on mirror-finished surfaces of the three test materials, in air, at loads which could be considered to sample the bulk deformation properties, namely,  $\approx 5$  N for the metals and 2.5 N for the glass. The

results are shown in Fig. 1. Each data point in this figure represents the mean and standard deviation of measurements from five impressions at a fixed input signal setting. Significant increases in hardness are observed with declining contact period for the three months, particularly for the tungsten and the glass. The trend for the latter is commensurate with that observed by Gunasekera and Holloway [7]. It is interesting to note that of the two metals studied it is the one with the lower melting point, copper, which is relatively insensitive to time variations.

The data contained in Fig. 1 are acknowledged to be restricted in several respects: the number of solids investigated is hardly large enough to allow general conclusions to be drawn concerning the role of material parameters in the deformation kinetics; the range of contact times is limited, such that any extrapolations into the realms of either dynamic impact or long-term loading would carry an element of extreme uncertainty; and no attempt has been made to control the environment. Nevertheless, the results serve to confirm that hardness can indeed be subject to rate effects. Furthermore, systematic study of such trends might be expected to throw some light on the micromechanics of the processes which control the deformation properties of materials.

#### Acknowledgements

The authors are grateful to E. R. Fuller for discussions on parts of this work, R. J. Fields and W. J. Boettinger for providing the tungsten specimen, and M. I. Cohen and C. S. Tilghman for experimental assistance. Funding for the study was provided by the US Office of Naval Research, Metallurgy and Ceramics Program.

#### References

1. "The Science of Hardness Testing and its Research Applications", Symposium Proceedings (American Society for Metals, Metals Park, Ohio, 1973).
2. T. O. MULHEARN and D. TABOR, *J. Inst. Met.* 89 (1960) 7.
3. A. G. ATKINS, A. A. DOS SILVERIO and D. TABOR, *ibid.* 94 (1966) 369.
4. W. W. WALKER and L. J. DEMER, *Trans. AIME* 230 (1964) 613.
5. W. W. WALKER, "The Science of Hardness Testing and its Research Applications" (American Society for Metals, Metals Park, Ohio, 1973).
6. J. H. WESTBROOK and P. J. JORGENSON, *Trans. AIME* 233 (1965) 425.

7. S. P. GUNASEKERA and D. G. HOLLOWAY, *Received 17 May*  
*Phys. Chem. Glasses* 14 (1973) 45.
8. D. M. MARSH, *Proc. Roy. Soc. Lond.* A279 (1964)  
420. *and accepted 26 May 1982*

4. E.R. Fuller, B.R. Lawn and R.F. Cook, "Theory of Fatigue for Brittle Flaws Originating from Residual Stress Concentrations," J. Am. Ceram. Soc. 66, 314-321 (1983).

# Theory of Fatigue for Brittle Flaws Originating from Residual Stress Concentrations

EDWIN R. FULLER\* and BRIAN R. LAWN\*

Fracture and Deformation Division, National Bureau of Standards, Washington, DC 20234

ROBERT F. COOK\*

Department of Applied Physics, School of Physics, University of New South Wales, New South Wales 2033, Australia

A theory is formulated for the general fatigue response of brittle flaws which experience residual stress concentrations. The indentation crack is taken as a model flaw system for the purpose of setting up the basic fracture mechanics equations, but the essential results are expected to have a wider range of applicability in the strength characterization of ceramics. A starting fatigue differential equation is first set up by combining an appropriate stress intensity factor for point- or line-contact flaws with a power-law crack velocity function. Analytical solutions are then obtained for the case of static fatigue. The resulting relation between lifetime and failure stress is shown to have exactly the same power-law form as the conventional solution for Griffith (residual-stress-free) flaws. This "equivalence" is used as a basis for extending the results to dynamic fatigue. A comparison of these analytical solutions with numerical counterparts defines the limits of accuracy of the theoretical procedure. However, while the form of the lifetime relation remains invariant, the values of the exponent and coefficient differ significantly for flaws with and without residual stress. Accordingly, the application of conventional fatigue theory to evaluate crack velocity parameters, without due regard for the nature of the critical flaw, can lead to serious errors. Explicit conversion formulas are given for transforming "apparent" velocity parameters for indentation flaws directly into "true" parameters. The implications of these results concerning the use of the indentation method for materials evaluation are discussed.

## I. Introduction

IT IS well recognized that the failure of brittle materials is governed by the micromechanics of crack growth from small flaws, and that chemical enhancement of this crack growth can cause significant reductions in the strength with increasing time under load. Embodied in the conventional fracture mechanics approach to "fatigue" phenomena of this kind<sup>1,2</sup> are three underlying assumptions: (a) The time dependence of the loading stresses, taken to act uniformly across the prospective crack plane, is specifiable; (b) the driving force on the extending crack is uniquely determined at any given characteristic length by these applied loading stresses; (c) the rate of crack extension is in turn uniquely determined by some well-defined function of the driving force for any given material/environment system. These assumptions allow one to write down a differential equation in crack length and time, the solution of which defines the stress conditions at failure. The widespread success enjoyed by the fracture mechanics formulation arises from the amenability to solutions in simple, closed form, which provide a convenient basis for lifetime predictions.

Apart from the clear-cut distinction made between loading at constant stress ("static fatigue") and constant stress rate ("dynamic fatigue"), surprisingly little attention has been devoted to the effects that potential variations in the starting equations may have in the lifetime analysis. Wiederhorn and Ritter<sup>3</sup> examined the crack

velocity function, and concluded that any of the commonly accepted empirical forms may fit fatigue data equally well (although extrapolations beyond the data range could lead to significant discrepancies in the predictions). Of the assumptions listed above, the second has been subjected to least scrutiny, it generally being assumed, without question, that the flaws respond in the classical "Griffith" sense; that is, the flaw is driven solely by the applied loading, this force increasing monotonically with the crack size until some instability condition is met.<sup>4,5</sup> It is thus implicit in the statement of the problem that any preexisting stresses which may have been responsible for generating the critical flaw in the first place<sup>5,6</sup> have long since ceased to be a significant contributing factor in the net driving force on the system.

However, recent studies of controlled flaws produced by indentation in strength test pieces have demonstrated that residual crack-generation stresses can have a profound influence on the crack evolution to failure.<sup>7</sup> The source of the residual field in this case is elastic-plastic mismatch at the boundary of the deformation zone which encases the sharp point and edges of the contacting body.<sup>8</sup> It then becomes necessary to incorporate a residual-contact term into the fracture mechanics equation for the crack driving force. Characteristically, this contribution *decreases monotonically* with crack size.<sup>8</sup> The resulting expression for the net force on the crack now takes on a considerably more complicated form. This complexity is such that the appropriate fatigue differential equation no longer appears to have simple analytic solutions. Accordingly, the first systematic investigations of residual-stress effects in fatigue, using results from dynamic<sup>9</sup> and static<sup>10</sup> loading tests on Vickers-indented soda-lime glass in water as a data base, were made by obtaining numerical solutions specific to one particular indenter/material/environment system. A subsequent analysis,<sup>11</sup> based on a reformulation of the differential equation in terms of judiciously normalized variables, allowed for generalization of the numerical procedure to include solutions for all possible systems. Most notably, this last study produced an empirical dynamic fatigue relation, for flaws satisfying a power-law crack velocity function, which was indistinguishable in form from that derived analytically for Griffith flaws. The exponents and coefficients in this relation were not, however, identical in the two cases; in particular, the values of the fatigue exponent, which for Griffith flaws is a direct measure of the corresponding exponent in the crack velocity function, differed by some 30%. A case study on a glass-ceramic<sup>12</sup> confirmed these and other features of the residual-stress theory, and outlined several unique advantages of the indentation method as a means for evaluating basic fatigue parameters.

One point that must be made at the outset is that indentation cracks should not be regarded simply as artificially introduced entities which bear no resemblance to strength-controlling flaws in real materials. There is growing evidence that the degrading surface damage which many ceramic components experience in finishing (e.g. machining)<sup>13</sup> or in service (sharp particle impact)<sup>14</sup> are characterized by the same residual stress effects as are indentation flaws. Indeed, the observation of strongly analogous local stress field effects about microstructural flaws in ceramics<sup>15</sup> suggests that the presence of residual crack driving forces may be the rule rather than the exception.

Viewed against this background the solution of the indentation fatigue problem takes on a broader significance. Accordingly, the

Received August 25, 1982; revised copy received December 27, 1982; approved January 3, 1983.

Supported by the Australian Research Grants Committee and the U. S. Office of Naval Research.

\*Member, the American Ceramic Society

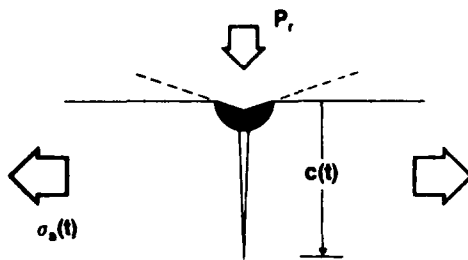


Fig. 1. Indentation flaw; crack of size  $c$  is formed at contact load  $P_r$  and subsequently subjected to applied tensile stress  $\sigma_a$ . Deformation zone about contact gives rise to residual stress field which contributes to crack driving force.

numerical base of the earlier analyses<sup>9-12</sup> must be seen as restrictive. Ideally, one would like to be able to obtain analytical solutions of the master differential equation in its most general possible form. Such solutions would provide a sounder basis for making intercomparisons between (a) flaws of different geometry, e.g. "point" flaws produced in normal loading vs "line" flaws produced in sliding loading; (b) different crack velocity functions; (c) static vs dynamic fatigue. In this paper we present an analysis which meets this ideal at least in part, the greatest restrictions being the need to retain a power-law crack velocity function and to obtain the dynamic fatigue solutions by an "equivalence" argument. The ensuing fatigue relation between lifetime and failure stress confirms the findings of the previous empirical studies, but now provides more explicit expressions for obtaining crack velocity parameters from fatigue plot slopes and intercepts.

II. Analytical Solution of Fatigue Differential Equation for Constant Applied Stress

(1) The Stress Intensity Factor and the Inert Strength

The key step in generalizing the Griffith-flaw concept to include residual-stress effects is an appropriate expression for the crack driving force. The essential variables expected to appear in any such expression are depicted in Fig. 1:  $c$  is the characteristic crack size,  $P_r$  the indentation load which determines the level of the residual field, and  $\sigma_a$  the subsequently applied tensile stress which takes the system to failure. In this work we shall make a special distinction between the geometrical extremes of "point" and "line" flaws; the former defines a crack configuration of semicircular profile centered about a point-force contact ( $P_r$ =force), the latter a crack of straight front parallel to a line-force contact ( $P_r$ =force/length). We shall also assume that the cracks are "well developed," i.e. are large compared to the deformation zone from which these cracks initiate. Following our previous procedure,<sup>11</sup> the requisite crack driving force may be formulated in terms of the composite stress intensity factor

$$K = K_r + K_a \tag{1a}$$

where the terms

$$K_r = \chi_r P_r / c^{r/2} \tag{1b}$$

$$K_a = \psi_r \sigma_a c^{1/2} \tag{1c}$$

respectively represent the contributions from the residual contact field and the applied loading; here  $r=3$  for point flaws and  $r=1$  for line flaws;  $\chi_r$  and  $\psi_r$  are dimensionless parameters of the indentation stress field and the crack geometry, respectively. This formulation is subject to some modification due to the influence of such factors as secondary crack systems, spurious surface stress states, etc.; detailed discussion of these factors is available elsewhere,<sup>11</sup> and will consequently be pursued no further here.

Equation (1) has certain features which are pertinent to the fatigue analysis to follow. These features are evident in the plots of the function  $K(c)$  in Fig. 2 for both point and line flaws. The curves for fixed values of  $P_r$  and  $\sigma_a$  pass through a well-defined

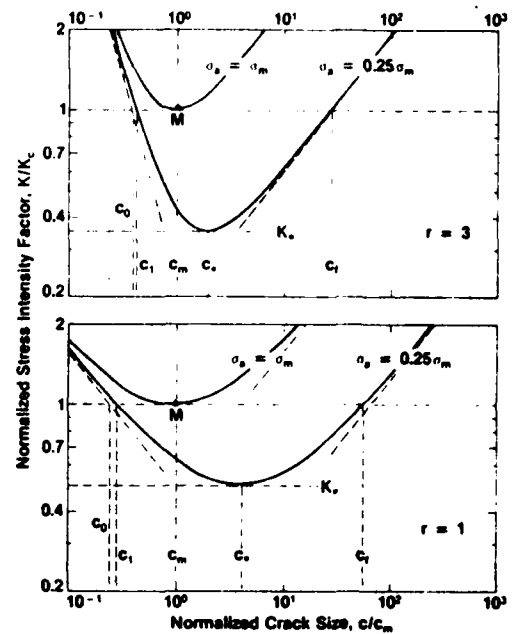


Fig. 2. Stress intensity factor as function of crack size (Eq. (1)) for point ( $r=3$ ) and line ( $r=1$ ) flaws. Inclined broken lines represent individual residual and applied components (Eqs. (1b) and (1c)); solid curves represent composite functions.

minimum, tending asymptotically on either side of this minimum to plots of the residual component of the stress intensity factor in the small-crack limit and of the applied component in the large-crack limit. The coordinate variables are normalized to the reference points  $M$ , which are of special significance in establishing baseline levels for the fatigue strength characterization<sup>11</sup>; in addition, this mode of plotting foreshadows the normalization scheme to be adopted in a later section of the paper. For arbitrary values of applied stress the condition  $dK/dc=0$  defines the minimum in Eq. (1), which we designate by asterisk notation:

$$K_* = (r+1)\chi_r P_r / c_*^{r/2} = [(r+1)/r]\psi_r \sigma_a c_*^{1/2} \tag{2a}$$

$$c_* = (r\chi_r P_r / \psi_r \sigma_a)^{2/(r+1)} \tag{2b}$$

The curves with their minimum at  $M$  correspond to the special case  $K_* = K_c$ ; at this point we may appropriately identify the critical variables  $\sigma_a = \sigma_m$ ,  $c_* = c_m$ , i.e.

$$\sigma_m = [r/(r+1)]^{r+1/2} K_c^{r+1/2} / \psi_r (\chi_r P_r)^{1/2} \tag{3a}$$

$$c_m = [(r+1)\chi_r P_r / K_c]^{2/r} \tag{3b}$$

It may be shown from Eqs. (2) and (3) that

$$K_*/K_c = (\sigma_a / \sigma_m)^{r/(r+1)} \tag{4a}$$

$$c_*/c_m = (\sigma_m / \sigma_a)^{2/(r+1)} \tag{4b}$$

so that as  $\sigma_a$  drops below  $\sigma_m$  the position of the minimum in Fig. 2 displaces downward and to the right relative to  $M$ .

The points at which the curves in Fig. 2 intersect the horizontal line  $K = K_c$  correspond to equilibrium crack configurations, stable or unstable according to whether the branches have negative or positive slope. The stable equilibria define appropriate initial conditions for ensuing fatigue fracture;  $c_0$  for loading at constant stress rate,  $c_1$  at constant stress. In practice, fatigue effects will be manifest in the postindentation crack configuration before application of tensile loading, causing subcritical extension from  $c_0$  to some non-equilibrium size  $c'_0$  (which may or may not exceed  $c_1$ ). The unstable equilibria at  $c_r$  define the final configuration immediately prior to the onset of catastrophic failure. It is useful at this stage to point out that an instability configuration can be achieved without ever departing from an equilibrium state, by steadily increasing the

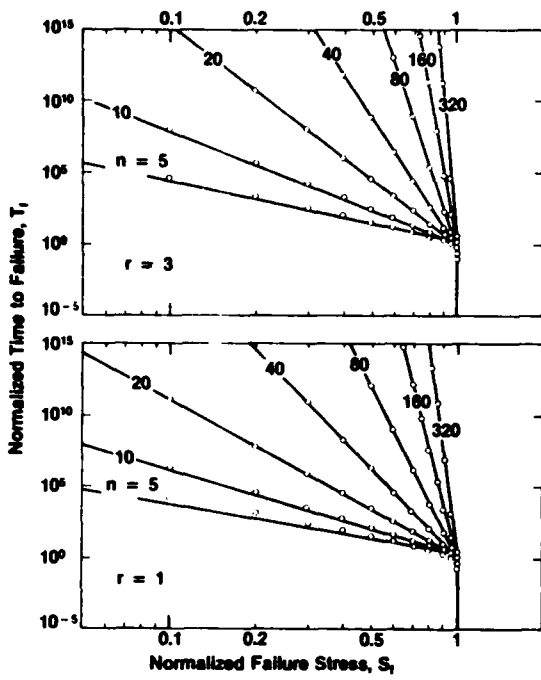


Fig. 3. Normalized plots of lifetime vs failure stress for point and line flaws; static fatigue results. Data points and solid lines represent numerical and analytical solutions of master fatigue differential equation, respectively. Note inert strength cutoff at  $S_f = 1 = S_i$ .

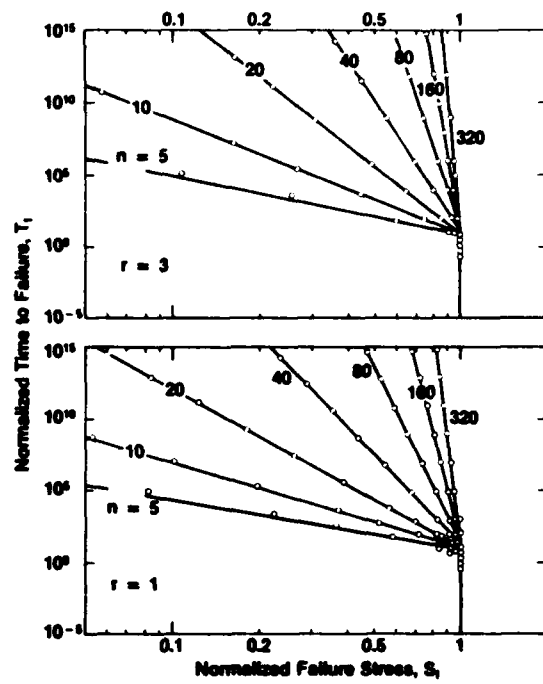


Fig. 4. Normalized plots of lifetime vs failure stress for point and line flaws; dynamic fatigue results. Data points and solid lines represent numerical and analytical solutions, respectively.

applied stress  $\sigma_a$  from zero to  $\sigma_m$ , thereby causing the crack to grow stably from  $c_0$  to  $c_m$ ; this takes us along  $K = K_c$  to point  $M$  in Fig. 2, where  $c_1$  merges with  $c_f$  to produce spontaneous failure. Since such conditions are most closely met in nonreactive test environments we may define an "inert" strength  $\sigma_i = \sigma_m$ , which from Eq. (3) can be written in the form

$$\sigma_i = [r/(r+1)]K_c / \psi_i c_i^{1/2} \quad (5)$$

independent of initial crack size.

For comparison, the corresponding inert strength  $\sigma_i^0$  for Griffith flaws follows from Eq. (1) in the limit of  $\chi_r = 0$ , with spontaneous failure occurring, without any precursor crack growth, at  $c_i$ , say:

$$\sigma_i^0 = K_c / \psi_i c_i^{1/2} \quad (6)$$

In this case the strength is, of course, sensitive to the initial flaw size; the appropriate value of  $c_i$ , i.e.  $c_0$ ,  $c_0'$ , or  $c_1$  (or indeed any other such crack dimension), will depend on the nature of the mechanical, thermal, and/or chemical (or other) processes responsible for removing the residual contact field between crack formation and strength testing.

(2) Formulation and Solution of the Fatigue Equation

The fracture mechanics approach to the fatigue problem begins with the assumption that a crack velocity function may be written, for a given material/environment system, in the form  $v = v(K)$ . In combination with the stress intensity factor,  $K = K(r, P_r, \sigma_a, c)$ , in Eq. (1) and the specified time variation of the applied tensile field,  $\sigma_a = \sigma_a(t)$ , the velocity function assumes the form of a differential equation,  $dc/dt = v[r, P_r, \sigma_a(t), c]$ . This equation must be solved for the time-to-failure,  $t_f$ , needed to take the crack from  $c_i$  to  $c_f$ , at which point the stress level defines the fatigue strength,  $\sigma_a = \sigma_f$ . The primary objective of any such analysis is to determine the relation between  $\sigma_f$  and  $t_f$  (or some equivalent parameter, such as stress rate  $\dot{\sigma}_a$  in dynamic fatigue).

To proceed with the solution of the differential equation it is necessary, of course, to know the form of the crack velocity function. In this paper we adopt the simple power-law relation

$$v = v_0(K/K_c)^n \quad (7)$$

where  $v_0$  and  $n$  are empirical quantities. At the moment, this is the only one of the commonly used crack velocity functions for which we have been able to obtain analytical solutions for flaws with residual stress. Thus we obtain

$$dc/dt = (v_0/K_c^n) \{K[r, P_r, \sigma_a(t), c]\}^n \quad (8)$$

as our master starting equation.

(A) Griffith Flaws; Static and Dynamic Fatigue Solutions: The standard solutions of Eq. (8) for Griffith flaws are well known.<sup>1-3</sup> It is nevertheless instructive to include them here as a base for comparing later solutions. Inserting  $\chi_r = 0$  into Eq. (1) yields

$$dc/dt = (v_0/K_c^n) K_c^n = (v_0/K_c^n) [\psi_i \sigma_a(t) c^{1/2}]^n \quad (9)$$

The problem accordingly reduces to one of straightforward integration by separation of variables. For static fatigue, i.e.  $\sigma_a = \text{constant} = \sigma_f$ , Eq. (9) becomes simply

$$\int_0^{t_f} dt = [K_c^n / v_0 (\psi_i \sigma_f)^n] \int_{c_i}^{c_f} dc / c^{n/2} \quad (10)$$

The integrated result may be written in the form

$$t_f \sigma_f^n = \lambda_i \quad (11)$$

where, in the usual approximation  $(c_i/c_f)^{(n-2)/2} \ll 1$ , and in conjunction with Eq. (6), we obtain

$$\lambda_i = 2K_c^n / (n-2) v_0 \psi_i^n c_i^{(n-2)/2} = [2/(n-2)] \sigma_i^n c_i / v_0 \quad (12)$$

The appearance of  $c_i$  as the controlling crack size in Eq. (12) reflects the fact that the crack system spends the greater proportion of its time evolution to failure in the region of minimum driving force.

The corresponding solution for dynamic fatigue,<sup>1-3</sup> i.e. for  $\sigma_a = \dot{\sigma}_a t$  with constant  $\dot{\sigma}_a$ , can be expressed by the same power law as Eq. (11), but with  $\lambda_i$  replaced by  $\lambda_d$ , where

$$\lambda_d = (n+1)\lambda_i \quad (13)$$

(B) *Flaws with Residual Stress; Static Fatigue Solution:* For the general case where  $\chi_r \neq 0$  in Eq. (1), Eq. (8) becomes

$$dc/dt = (v_0/K_r^n)(K_r + K_a)^n \\ = (v_0/K_r^n)(\chi_r P_r/c^{r+2} + \psi_r \sigma_r(t)c^{1/2})^n \quad (14)$$

Integration by separation of variables is no longer straightforward as it was for Griffith flaws. Even in static fatigue, for which the right side of Eq. (14) contains no explicit terms in time, it is not immediately clear how the failure stress might be extracted from the integral and thereby related to lifetime. It was difficulties of this kind which motivated the numerical approach described in Ref. 11.

However, it can now be demonstrated that Eq. (14) does have an analytical solution at  $\sigma_r = \text{constant} = \sigma_f$ . Since the integrated lifetime is controlled at one extreme by  $K_r$  for small cracks ( $c \ll c_*$ ) and at the other extreme by  $K_a$  for large cracks ( $c \gg c_*$ ), it is appropriate to introduce a variable that defines the relative stress intensity factor at either extreme. We accordingly choose:

$$\xi = K_a/(K_r + K_a) \\ = 1/[1 + (\chi_r P_r/\psi_r \sigma_f)/c^{(r+1)/2}] \quad (15)$$

where  $\xi$  defines the fraction of the total stress intensity factor which is associated with the applied field, this fraction increasing monotonically with crack size. A second, important motivation for introducing this reduced variable is to convert the lifetime integral to a dimensionless form so as to display the applied stress and indentation load dependence separately. After considerable manipulation, Eq. (14) becomes

$$\int_0^y dt = \{ [2K_r^n/(r+1)v_0] / [(\psi_r \sigma_f)^{n+2\nu(r+1)} (\chi_r P_r)^{n-2\nu(r+1)}] \} \\ \times \int_{\xi_0}^{\xi_f} \xi^{r(n+2\nu(r+1)-1)} (1-\xi)^{n-2\nu(r+1)-1} d\xi \quad (16)$$

and we note that  $\sigma_f$  does indeed appear outside the integral. At this stage a significant simplification in the expression can be made by introducing the quantity

$$n' = (rn+2)/(r+1) \quad (17)$$

This will be seen later, with the benefit of hindsight, to be a particularly convenient choice of substitution. A further simplification is to assign the following values to the limits of integration in Eq. (16), consistent with our identification of the initial and final conditions in Fig. 2 and Eq. (15),

$$\xi_0 = \psi_r \sigma_f c_i^{1/2} / K_r \rightarrow 0 \quad (18a)$$

$$\xi_f = \psi_r \sigma_f c_f^{1/2} / K_r \rightarrow 1 \quad (18b)$$

in which case the integral in Eq. (16) reduces to the beta function.\* These value assignments are tantamount to saying that the initial conditions are governed by the residual component of the stress intensity factor, the final conditions likewise by the applied component. In any case, the final result is not expected to be sensitive to the limits of integration, bearing in mind that the region of minimum driving force in Fig. 2, which must control the fracture kinetics, lies intermediate to the initial and final configurations. This assumption is verified in the Appendix. With these simplifications Eq. (16) reduces to

$$t_f = [2K_r^n/(r+1)v_0] (\psi_r \sigma_f)^n (\chi_r P_r)^{n-n'} B(n', n-n') \quad (19)$$

with the beta function

$$B(n', n-n') = \int_0^1 \xi^{n'-1} (1-\xi)^{n-n'-1} d\xi \quad (20)$$

Thus the requisite relation between lifetime and failure stress has the familiar form

$$t_f \sigma_f^{n'} = \Lambda'_f \quad (21)$$

where we obtain, in conjunction with Eqs. (3) and (5),

$$\Lambda'_f = [2K_r^n/(r+1)v_0] (\psi_r \sigma_f)^n (\chi_r P_r)^{n-n'} B(n', n-n') \\ = [2(r+1)^{n-1}/r^n] B(n', n-n') \sigma_f^n c_m/v_0 \\ \cong [8\pi/(r+1)n']^{1/2} \sigma_f^n c_m/v_0 \quad (22)$$

the last expression arising from an asymptotic expansion of the beta function for large  $n'$  (Appendix).

While the form of Eq. (21) is indistinguishable from that of Eq. (11) for Griffith flaws, the exponent and coefficient are significantly modified. The implications of these modifications are discussed in Section IV.

### III. Comparison of Analytical and Numerical Solutions: Extension to Constant Stress-Rate Loading

It is instructive to examine the mutual consistency of the results obtained analytically in Section II and numerically in Ref. 11. To do this, and to broaden the scope of the treatment to date, numerical solutions, previously confined to the special case  $\dot{\sigma}_a = \text{constant}$  and  $r=3$ ,<sup>11</sup> are here generated for each combination of fatigue (static or dynamic) and flaw (point or line) types.

Following Ref. 11, reduced variables are introduced as follows:

$$S_a = \sigma_a/\sigma_m \quad (23a)$$

$$C = c/c_m \quad (23b)$$

$$T = tv_0/c_m \quad (23c)$$

Reference to Eq. (5) then allows the differential equation for flaws with residual stress, Eq. (14), to be expressed in a more universal form,

$$dC/dT = \{1/(r+1)C^{r+2} + [r/(r+1)]S_a(T)C^{1/2}\}^n \quad (24)$$

which is especially amenable to numerical analysis. This equation is solved by a stepwise integration procedure for the (reduced) time-to-failure  $T_f$  to take the crack from  $C_i$  (approximated by the value  $C_0 = 1/(r+1)^{2r}$  at  $S_a = 0$ ) to  $C_f$ .<sup>11</sup> The corresponding failure stress  $S_f$  at the critical end point of the integration is seen to be uniquely determined by the values of  $r$  and  $n$  and the form of the stressing function  $S_a(T)$ . It is noted that the normalization scheme conveniently relates all variables to the inert strength state, i.e.  $S_i = S_m = 1$  and  $C_m = 1$ , as represented by the reference point  $M$  in Fig. 2.

To facilitate the required comparisons, let us translate the essential results of the analytical treatment in Section II into reduced variable notation. Taking static fatigue first, i.e.  $S_a = \text{constant} = S_r$ , Eq. (21) retains its basic form,

$$T_f S_f^{n'} = \Lambda'_f \quad (25)$$

with the coefficient relating to its counterpart in Eq. (22) as

$$\Lambda'_f = \lambda'_f v_0/\sigma_f^n c_m \\ = [2(r+1)^{n-1}/r^n] B(n, n-n') \\ \cong [8\pi/(r+1)]^{1/2} / n'^{1/2} \quad (26)$$

where the last line in this equation is an asymptotic approximation in  $n'$  (Appendix).

At this point, it is pertinent to recall the essential equivalence of the static fatigue solutions for flaws with and without residual stress, Eqs. (21) and (11). It would appear reasonable to expect this equivalence to extend to dynamic fatigue,  $S_a = S_a T$  ( $S_a$  constant). Accordingly, since in the case of Griffith flaws the static and dynamic solutions can be shown analytically to have exponents which are identical and coefficients which relate linearly via Eq. (13), we may proceed by analogy and modify Eq. (25), thus

$$T_f S_f^{n'} = \Lambda'_d \quad (27)$$

where we have from Eq. (26)

$$\Lambda'_d = \lambda'_d v_0/\sigma_f^n c_m = (n'+1)\Lambda'_f \cong [8\pi/(r+1)]^{1/2} n'^{1/2} \quad (28)$$

with the same asymptotic approximation as made in Eq. (26).

Figures 3 and 4 show the results of both analytical and numerical

\*See any standard text on advanced mathematical methods.

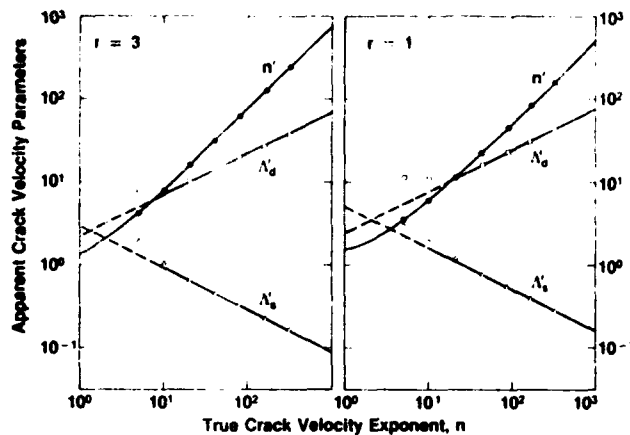


Fig. 5. Plots showing variation of exponent  $n'$  ( $n'_p$  and  $n'_l$  cannot be distinguished in these plots) and coefficients  $\Lambda'_p$  and  $\Lambda'_l$  with  $n$ , for point and line flaws. Data points and solid lines represent numerical and analytical evaluations, respectively.

calculations on logarithmic plots of lifetime vs failure stress for static and dynamic fatigue, respectively, and for point and line flaws. The data points in these plots are numerical evaluations of Eq. (24) at either fixed  $S_0$  (Fig. 3) or  $\dot{S}_0$  (Fig. 4) for selected values of  $n$ . The corresponding solid lines are analytical representations of Eqs. (25) and (27), in conjunction with Eq. (17). The degree of correlation between data points and solid curves reflects the accuracy of the theory developed in Section II. In this context the tendency for systematic departures to increase at low  $n$  (or  $n'$ ) values may be taken as a measure of the range of validity of the asymptotic beta function expansion used in the evaluation of the integral in Eq. (16). Special note may be made of the fact that the correlations appear to be as strong for the dynamic fatigue results in Fig. 4 as for the static fatigue in Fig. 3, thereby providing some justification for the equivalence argument adopted to extend the theoretical analysis earlier in this section.

A more detailed comparison of results is obtained by considering the specific variations of the exponent  $n'$  and coefficients  $\Lambda'$  in Eqs. (25) and (27) with  $n$ . This is done in Fig. 5 for point and line flaws. The data points again represent numerical evaluations of Eq. (24), obtained from slope and intercept evaluations in the "linear" region of the lifetime vs failure stress plots; the solid curves likewise represent analytical evaluations from Eqs. (17), (26), and (28). The disagreement between the two approaches is  $<1\%$  for the exponent and  $<10\%$  for the coefficients in the domain  $n > 10$ .

#### IV. Discussion

The formulation presented in this paper demonstrates that analytical solutions can be obtained to the fracture mechanics fatigue equations for flaws which are subject to residual-contact driving forces and which extend according to a power-law crack velocity function. A major feature of these solutions is the fact that they are identical in basic form to those obtained for Griffith flaws in conventional fatigue analysis. Thus, from a standard linear plot of lifetime vs failure stress in logarithmic coordinates it would not be possible to determine, without independent information on the crack velocity parameters, whether the flaws in a given material/environment system are or are not influenced by residual stresses. This conclusion should provide some comfort to those who have advocated the exclusive use of strength data for predicting component lifetimes, since the nature of the flaw now does not enter into consideration (unless perhaps the predictions require extrapolation beyond the data range<sup>10</sup>). Of particular importance in this context is the widely proposed use of dynamic fatigue testing as the source of base data for design requirements; in terms of a lifetime vs failure stress diagram the curve for static loading generates from that for dynamic loading via a simple connecting relation for the

intercepts. To illustrate, Fig. 6 shows data from both dynamic<sup>10</sup> and static<sup>10</sup> fatigue test runs on indented soda-lime glass in water. A least-squares fit through the dynamic fatigue data gives  $n'$ , Eq. (27); subsequent translation downward through  $\log(n'+1)$ , Eq. (28), generates the static fatigue curve. The agreement between prediction and observation in the latter case, notwithstanding the experimental scatter, may be taken as a justification for the "equivalence" argument used to infer the existence of Eqs. (27) and (28) from their Griffith counterparts, Eqs. (11) and (13).

There is, however, considerable danger in analyzing fatigue results from materials whose flaw characteristics are not known. This is particularly so if one attempts to relate the strength data to the parameters in the crack velocity function. The point is most readily demonstrated by considering the exponent in this function in terms of the slope of lifetime vs failure stress plot. From Eq. (11) for Griffith flaws the slope gives  $n$  (more strictly, its negative) directly, whereas from Eq. (21) for flaws with residual stress the corresponding slope is  $n'$ ; in the latter case evaluation of the true exponent requires inversion of Eq. (17):

$$n = 4n'/3 - 2/3 \quad (r=3) \quad (29a)$$

$$n = 2n' - 2 \quad (r=1) \quad (29b)$$

Thus substantial errors may be incurred if the conventional theory of fatigue is used to analyze data for contact-induced flaws which have undergone no subsequent stress relaxation. For example, in Fig. 6 the apparent exponent is determined at  $n' = 13.7 \pm 0.2$ , whence Eq. (29a) appropriate to point (Vickers-induced) flaws predicts  $n = 17.6 \pm 0.3$ ; this latter value is close to the true exponent  $n = 17.9 \pm 0.5$  obtained from comparative tests on indented specimens subjected to an anneal treatment prior to strength testing,<sup>9</sup> and lies in the range of  $16 < n < 19$  generally found for large-scale cracks in the system soda-lime-glass/water.<sup>16</sup> The discrepancy between apparent and true exponents is predicted to be even greater for linear flaws, almost a factor of 2, Eq. (29b). It is interesting to note that discrepancies of this order were found by Pletka and Wiederhorn<sup>17</sup> in certain ceramics where machining damage provided the strength-controlling flaws.

Similar care must be exercised in evaluating the coefficient of the crack velocity function from the intercept on a fatigue plot. For flaws with residual stress, inversion of Eqs. (26) and (28) gives

$$v_0 = \Lambda' \sigma_r^n c_m / \Lambda' \quad (30)$$

where

$$\Lambda'_p = (2\pi/n')^{1/2} \quad (\sigma_a = \text{constant}, r=3) \quad (31a)$$

$$\Lambda'_l = (4\pi/n')^{1/2} \quad (\sigma_a = \text{constant}, r=1) \quad (31b)$$

$$\Lambda'_p = (2\pi n')^{1/2} \quad (\dot{\sigma}_a = \text{constant}, r=3) \quad (31c)$$

$$\Lambda'_l = (4\pi n')^{1/2} \quad (\dot{\sigma}_a = \text{constant}, r=1) \quad (31d)$$

Inversion of the corresponding intercept relations for Griffith flaws, Eqs. (12) and (13), leads to an analogous result, but with a different  $\Lambda'$  term and with  $c_i$  replacing  $c_m$  as the controlling crack parameter.

We should emphasize here that Eq. (31) represents only a first-order approximation; additional terms in a series expansion may be required where accuracy requirements are stringent (Appendix). However, since lifetimes are generally plotted in logarithmic coordinates the present approximation will usually suffice, except perhaps at  $n \leq 10$ .

This sensitivity of the slope and intercept terms in the fatigue relations to the nature of the strength-controlling flaw provides a strong case for the use of indentation testing in the evaluation of crack velocity parameters. Any uncertainty as to whether the cracks are subject to residual stress effects and whether the cracks have essential point or line (or intermediate) geometry is then eliminated. Of course, such elements of uncertainty can hardly be avoided in ceramic components which are to be placed in service, so any attempt to apply the above procedure in reverse, i.e. to use macroscopically determined crack velocity parameters to predict lifetime characteristics, needs to be treated with extreme caution.

Indeed, the present results would appear to strengthen the case for fatigue testing on the actual surface finish to be used in service.

Thus far in the discussion we have effectively been considering the fatigue response of a given material/environment system at fixed indentation loading conditions. How might the formalism developed here be rearranged to accommodate a test program which calls for the removal of these restrictions? Ideally, it would be convenient to be able to devise a scheme whereby all data for a given system could be plotted onto a universal curve, regardless of load, such that comparative evaluations could be readily made for different materials. Alternatively, one could use load as a control variable for investigating the effect of flaw size on the validity of crack growth laws.<sup>11</sup> Accordingly, inserting Eq. (30) into the general fatigue relation  $t_f \sigma_f^n = \lambda'$  gives<sup>7</sup>

$$t_f / \lambda' c_m = (1/v_0)(\sigma_f / \sigma_f)^n \tag{32}$$

The load  $P$  may now be introduced explicitly into the analysis via Eq. (3) by writing

$$\sigma_f = \sigma_m = \zeta / P_f^{1/r} \tag{33a}$$

$$c_m = \eta P_f^{2/r} \tag{33b}$$

where  $\zeta = \zeta(r, \chi, \psi, K_c)$  and  $\eta = \eta(r, \chi, K_c)$  are experimentally measurable inert-strength constants.<sup>12</sup> Then Eq. (32) becomes

$$t_f / P_f^{2/r} = (\lambda' \zeta^n \eta / v_0) / (\sigma_f P_f^{1/r})^n \tag{34}$$

so plots of  $t_f / P_f^{2/r}$  vs  $\sigma_f P_f^{1/r}$  in logarithmic coordinates should produce universal straight lines for individual material/indenter systems. These plots are, of course, nothing more than generalized versions of those illustrated in Fig. 6. The advantage of this scheme is that it provides the basis for constructing "master diagrams" in which the relative fracture properties of different materials are immediately apparent. Thus the slope of any such plot in the fatigue region gives a direct measure of the "susceptibility" to delayed failure, in the manner already discussed in relation to Fig. 6; the inert-strength cutoff likewise gives a measure of the intrinsic "toughness," as reflected by the parameter  $\zeta$  in Eq. (33a). Clearly, the materials with superior strength characteristics will be those which, for a specified lifetime domain, lie to the right of the diagram. Further details of this proposed scheme will be explored elsewhere.<sup>13</sup>

There are in the analysis several implicit assumptions which have not been given close attention in the body of the text. These include: (a) that the solutions of the fatigue differential equations are insensitive to initial conditions, (b) that the multiple-region effects in the crack velocity function are negligible, (c) that the test material is free of preexisting surface stresses. Reference 11 contains a detailed discussion of these points.

Finally, although our attention has focused on indentation cracks the basic stress-intensity formulation of Eq. (1) might be expected to cover a far broader range of flaw types. Similarities in the local residual stress fields about microstructural defects in ceramics (due to strain incompatibilities at grain or inclusion boundaries) and indentations have already been noted by Green.<sup>14</sup> Extension to these other cases is accordingly a simple matter of reinterpreting the physical meaning of the quantity  $\chi, P$  in Eq. (15) in terms of characteristic pressure and radius parameters which define the intensity and extent of the field.<sup>15</sup> Then, provided of course that the reactive chemical species has access to the defect centers to cause fatigue in the first place, the conventional analysis of lifetime properties is subject to precisely the same modifications as described for contact flaws in Sections II and III.

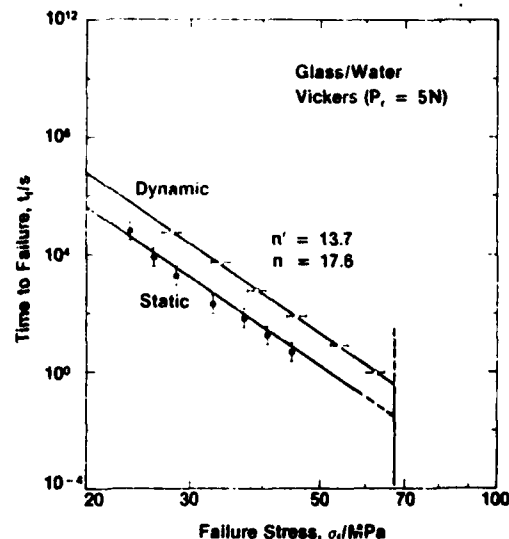


Fig. 6. Plot comparing static and dynamic fatigue response for soda-lime glass in water using indentation flaws. Data from Refs. 9 and 10, standard deviation error bars.

APPENDIX

Lifetime Integral and its Approximations

In this appendix the assumptions made in the derivation of the lifetime formulation for cracks in combined residual and applied stress fields are examined. Specific attention is directed to the dimensionless quantity in Eq. (26),

$$\Lambda'_i = [2(r+1)^{n-1} / r^n] \int_{\xi_i}^{\xi_f} \xi^{n-1} (1-\xi)^{n-n'} d\xi \tag{A-1}$$

where the integral is the generalized version of Eq. (20) (i.e. with variable limits of integration). Consideration of this one expression is sufficient to cover all the approximations referred to in Sections II(2B) and III. The treatment here is taken in two parts: in the first,  $\Lambda'_i$  is expressed in terms of the beta function and two incomplete beta functions, and these functions are evaluated to determine their relative importance; in the second part, the beta function, which is confirmed to be the dominant term in  $\Lambda'_i$ , is expanded in an asymptotic series for large values of  $n$ .

An important point to keep in mind here is that accuracy in  $\Lambda'_i$ , although clearly desirable, is not nearly as critical as it is in the exponent  $n'$  in Eq. (25), for which we have an exact expression (Eq. (17)). Generally, accuracy to within a factor of two in  $\Lambda'_i$  is adequate for most lifetime and crack velocity evaluations.

(1) Beta Function Expression

The integral in Eq. (A-1) may be rewritten as follows:

$$\int_{\xi_i}^{\xi_f} \xi^{n-1} (1-\xi)^{n-n'} d\xi = \int_0^1 \xi^{n-1} (1-\xi)^{n-n'} d\xi - \int_0^{\xi_i} \xi^{n-1} (1-\xi)^{n-n'} d\xi - \int_{\xi_f}^1 \xi^{n-1} (1-\xi)^{n-n'} d\xi \tag{A-2}$$

The first integral is the beta function  $B(n', n-n')$  as previously defined in Eq. (20). The second and third integrals are the incomplete beta functions<sup>20</sup>  $B_{\xi_i}(n', n-n')$  and  $B_{1-\xi_f}(n-n', n')$  (using a transformation of variables  $\xi \rightarrow 1-\xi'$  in the latter case). Equation (A-1) then becomes

$$\Lambda'_i = [2(r+1)^{n-1} / r^n] [B(n', n-n') - B_{\xi_i}(n', n-n') - B_{1-\xi_f}(n-n', n')] \tag{A-3}$$

It may be noted in passing that if we were to define a dimensionless velocity  $v = V c_m / t_f$  and stress intensity factor  $K = \sigma_f / \sigma$ , Eq. (32) could be inverted to give  $v = v_0 K^n$ . In this interpretation the plotting scheme to be proposed may be regarded as representative of an inverse crack velocity function

**Table IA. Initial and Final Values of Reduced Stress Intensity Factor,  $\xi=K_a/K$ , for Selected Values of Reduced Applied Stress,  $S_a=\sigma_a/\sigma_m$**

Flaw type	$S_a$	$\xi_i$	$\xi_f$
Point ( $r=3$ )	0.9	0.559	0.891
	0.7	0.390	0.959
	0.5	0.261	0.986
	0.3	0.150	0.997
	0.1	0.048	1.000
Line ( $r=1$ )	0.9	0.342	0.658
	0.7	0.226	0.774
	0.5	0.146	0.854
	0.3	0.082	0.918
	0.1	0.026	0.974

**Table IIA. Comparison of  $\Lambda'_i$  Evaluations from Equation (A-3) Using Beta Function Contribution Only and Full Expression**

Flaw type	$n$	$n'$	$\Lambda'_i$ (beta)	$S_a$	$\Lambda'_i$
Point ( $r=3$ )	10	8	1.110	0.9	0.780
				0.7	1.051
				0.3	1.110
				0.9	0.659
				0.7	0.751
	18	14	0.755	0.9	0.659
				0.7	0.751
				0.5	0.755
				0.9	0.482
				0.7	0.492
	38	29	0.492	0.9	0.482
				0.7	0.492
				0.9	0.482
				0.7	0.492
				0.9	0.482
Line ( $r=1$ )	10	6	2.032	0.9	1.181
				0.7	1.768
				0.1	2.032
				0.9	1.045
				0.7	1.315
	18	10	1.348	0.9	1.045
				0.7	1.315
				0.3	1.348
				0.9	0.813
				0.7	0.864
	38	20	0.864	0.9	0.813
				0.7	0.864
				0.9	0.813
				0.7	0.864
				0.9	0.813

The beta function in Eq. (A-3) is readily computed from the more familiar gamma function to which it is related<sup>20</sup>; generally,

$$B(n', n-n') = \Gamma(n')\Gamma(n-n')/\Gamma(n) \quad (\text{A-4a})$$

or, more simply, when both  $n$  and  $n'$  are integers,

$$B(n', n-n') = (n'-1)!(n-n'-1)!/(n-1)! \quad (\text{A-4b})$$

Computation of the *incomplete* beta functions, however, requires prior specification of the reduced quantities  $\xi_i$  and  $\xi_f$ . In the same way as the limiting values of these two quantities in Eq. (18) are derived from the defining relation Eq. (15), we may write,

$$\xi = [r/(r+1)]S_a C^{1/r} \quad (\text{A-5})$$

where we have invoked the normalizing scheme of Eq. (23). For present purposes we can adequately illustrate the approximations involved by considering the relatively simple case of static fatigue, i.e.  $S_a = \text{constant}$ ; values of  $\xi_i$  and  $\xi_f$  appropriate to initial and final crack sizes are then obtained from the roots of Eq. (1) at  $K=K_c$  (again expressed in normalized form). Table IA shows values for several reduced applied stresses for both point and line flaws. These values can clearly differ substantially from the limits of  $\xi_i=0$  and  $\xi_f=1$  of Eq. (18), particularly at stress levels approaching the inert strength  $S_a=1$ .

In our study the incomplete beta functions have been evaluated using an adaptive Simpson's rule computer code for the integration limits of Table IA, although algorithms are available for analytical (but tedious) computation.

Table IIA summarizes the results of the calculations, for selected values of  $n$  and for point and line flaws. The tabulation compares evaluations of  $\Lambda'_i$  made with the incomplete beta functions omitted

**Table IIIA. Comparison of  $\Lambda'_i$  Evaluations from Equation (A-9) Using Lead Term and Full Beta Function Expression**

Flaw type	$n$	$n'$	$[8\pi/(r+1)n']^{1/2}$	$\Lambda'_i$ (beta)
Point ( $r=3$ )	10	8	0.886	1.110
	18	14	0.670	0.755
	38	29	0.465	0.492
	78	59	0.326	0.335
	158	119	0.230	0.233
Line ( $r=1$ )	10	6	1.447	2.032
	18	10	1.121	1.348
	38	20	0.793	0.864
	78	40	0.560	0.584
	158	80	0.396	0.405

and included. It is clear that the terms containing these incomplete beta functions make a significant contribution only at low  $n$  and high  $S_a$ . Even in these worst cases the discrepancy is generally likely to be less than the factor of two tolerance level quoted earlier. Thus in the region of larger  $n$  (which appears to pertain to most practical ceramics) and long lifetimes,  $\Lambda'_i$  effectively becomes an invariant quantity, independent of applied stress.

### (2) Asymptotic Expansion of Beta (Gamma) Function

In the spirit of the approximations above in which only the beta function is retained in Eq. (A-3) we have

$$\Lambda'_i = [2(r+1)^{n-1}/r^n] \Gamma(n')\Gamma(n-n')/\Gamma(n) \quad (\text{A-6})$$

The gamma functions in this expression may now be expanded using Stirling's formula<sup>20</sup>; e.g. for the first gamma function

$$\ln \Gamma(n') \sim \ln(2\pi/n')^{1/2} + n' \ln n' - n' + S(n') \quad (\text{A-7})$$

where  $S(n')$  is the series

$$S(n') = \sum_{k=1}^{\infty} [B_{2k}/2k(2k-1)]/n'^{2k-1} \quad (\text{A-8})$$

with  $B_{2k}$  the Bernoulli numbers ( $B_2=1/6$ ,  $B_4=-1/30$ , etc.).<sup>20</sup> After some manipulation, Eq. (A-6) reduces to

$$\begin{aligned} \ln \Lambda'_i \sim & \ln [8\pi/(r+1)n']^{1/2} \\ & + n' \ln [n'/(n'-2)] - (n-1/2) \ln [n/(n-2)] \\ & + S(n') - S(n) + S(n-n') \end{aligned} \quad (\text{A-9})$$

In this expression the second and third terms tend to cancel and the series  $S$  terms become small as  $n$  increases, leaving the lead term as the dominant quantity. The accuracy with which this lead term can be used to represent  $\Lambda'_i$  may be gauged from Table IIIA.

**Acknowledgments:** The authors thank T. J. Chuang and E. D. Case for assistance with the calculations in the Appendix.

### References

- S. M. Wiederhorn, pp. 613-46 in *Fracture Mechanics of Ceramics*, Vol. 2. Edited by R. C. Bradt, D. P. H. Hasselman, and F. F. Lange. Plenum, New York, 1974.
- A. G. Evans and S. M. Wiederhorn, "Proof Testing of Ceramic Materials: An Analytical Basis for Failure Prediction," *Int. J. Fract.*, **10** [3] 379-92 (1974).
- S. M. Wiederhorn and J. E. Ritter, pp. 202-14 in *Fracture Mechanics Applied to Brittle Materials*. Edited by S. W. Frieman. *ASTM Spec. Tech. Publ.*, No. 678, 1979.
- A. A. Griffith, "Phenomena of Rupture and Flow in Solids," *Philos. Trans. R. Soc. (London) Ser. A.*, **221** [4] 163-98 (1920).
- B. R. Lawn and T. R. Wilshaw, *Fracture of Brittle Solids*, Chs. 2 and 3. Cambridge University Press, London, 1975.
- A. H. Cottrell, "Theory of Brittle Fracture in Steel and Similar Metals," *Trans. Met. Soc.*, **212** [3] 192-203 (1958).
- (a) D. B. Marshall and B. R. Lawn, "Residual Stress Effects in Sharp-Contact Cracking: I," *J. Mater. Sci.*, **14** [8] 2001-12 (1979).
- (b) D. B. Marshall, B. R. Lawn, and P. Chantikul, "Residual Stress Effects in Sharp-Contact Cracking: II," *J. Mater. Sci.*, **14** [9] 2225-35 (1979).
- B. R. Lawn, A. G. Evans, and D. B. Marshall, "Elastic/Plastic Indentation Damage in Ceramics: The Median/Radial Crack System," *J. Am. Ceram. Soc.*, **63** [9-10] 574-81 (1980).
- D. B. Marshall and B. R. Lawn, "Flaw Characteristics in Dynamic Fatigue: The Influence of Residual Contact Stresses," *J. Am. Ceram. Soc.*, **63** [9-10] 532-36 (1980).

<sup>10</sup>P. Chantikul, B. R. Lawn, and D. B. Marshall, "Micromechanics of Flaw Growth in Static Fatigue: Influence of Residual Contact Stresses," *J. Am. Ceram. Soc.*, **64** [6] 322-25 (1981).

<sup>11</sup>B. R. Lawn, D. B. Marshall, G. R. Anstis, and T. P. Dabbs, "Fatigue Analysis of Brittle Materials Using Indentation Flaws: I," *J. Mater. Sci.*, **16** [10] 2846-54 (1981).

<sup>12</sup>R. F. Cook, B. R. Lawn, and G. R. Anstis, "Fatigue Analysis of Brittle Materials Using Indentation Flaws: II," *J. Mater. Sci.*, **17** [4] 1108-16 (1982).

<sup>13</sup>D. B. Marshall; unpublished work.

<sup>14</sup>D. B. Marshall and B. R. Lawn, "Residual Stresses in Dynamic Fatigue of Abraded Glass," *J. Am. Ceram. Soc.*, **64** [1] C-6-C-7 (1981).

<sup>15</sup>D. J. Green, in *Fracture Mechanics of Ceramics*. Edited by R. C. Bradt, D. P. H. Hasselman, F. F. Lange, and A. G. Evans. Plenum, New York, 1982.

<sup>16</sup>S. M. Wiederhorn; unpublished work.

<sup>17</sup>B. J. Pietka and S. M. Wiederhorn, "A Comparison of Failure Predictions by Strength and Fracture Mechanics Techniques," *J. Mater. Sci.*, **17** [5] 1247-68 (1982).

<sup>18</sup>T. D. Dabbs, B. R. Lawn, and P. L. Kelly, "A Dynamic Fatigue Study of Soda-Lime and Borosilicate Glasses Using Small-Scale Indentation Flaws," *Phys. Chem. Glasses*, **23** [2] 58-66 (1982).

<sup>19</sup>R. F. Cook and B. R. Lawn; unpublished work.

<sup>20</sup>I. S. Gradshteyn and I. M. Ryzhik, *Table of Integrals, Series and Products*. Chs. 8, 9. Academic Press, New York, 1980.

**END**

**FILMED**

**10-83**

**DTIC**